

UC Riverside

2018 Publications

Title

Navigation With Cellular CDMA Signals- Part II: Performance Analysis and Experimental Results

Permalink

<https://escholarship.org/uc/item/6jf2t5qz>

Journal

IEEE Transactions on Signal Processing, 66(8)

ISSN

1053-587X 1941-0476

Authors

Khalife, Joe
Kassas, Zaher M

Publication Date

2018-04-15

DOI

10.1109/TSP.2018.2799166

Peer reviewed

Navigation With Cellular CDMA Signals—Part II: Performance Analysis and Experimental Results

Joe Khalife¹, *Student Member, IEEE*, and Zaher M. Kassas², *Senior Member, IEEE*

Abstract—A framework for navigation using cellular code division multiple access (CDMA) signals is studied in this paper. Theoretical lower bounds on the navigation performance using pseudorange measurements drawn from the cellular CDMA base transceiver stations (BTSs) are derived. Moreover, the navigation performance for a mapper/navigator framework is studied in the presence of timing discrepancies between the mapper and navigator. In this framework, a mapping receiver (mapper) estimates the stochastic dynamic clock biases of the BTSs and shares these estimates with a navigating receiver (navigator). The optimal navigation performance of the mapper/navigator framework in the presence of timing discrepancies is analyzed, and a practical upper bound on the resulting position error is derived. Experimental results for a ground vehicle and unmanned aerial vehicles (UAVs) are presented. The ground vehicle results show a mean distance difference of 5.51 m between the cellular CDMA-only navigation solution and a GPS navigation solution in the absence of clock bias discrepancies. The UAV results show an improvement of 10.57 m in the root-mean-square error of the cellular CDMA navigation solution, when the sector clock bias discrepancies are accounted for utilizing the statistical model relating observed clock biases from different sectors of the same BTS cell.

Index Terms—Radionavigation, signals of opportunity, opportunistic navigation, direct-sequence code-division multiple access, wireless sensor networks.

I. INTRODUCTION

EXPLOITING ambient radio frequency (RF) signals of opportunity (SOPs) for positioning and navigation in environments where global navigation satellite system (GNSS) signals are not usable (e.g., in deep urban canyons [1] and under jammed and spoofed situations [2], [3]) has received considerable attention recently [4]–[7]. The literature on SOPs answers theoretical questions on the observability and estimability of the SOP signal landscape [8], [9], motion planning in the SOP signal landscape for optimal information gathering [10]–[12], and collaborative SOP landscape map building [13]. Moreover, different studies have been conducted for specific types of

SOPs including AM/FM radio [14], [15], iridium satellites [16], [17], digital television [18], [19], cellular [20]–[25], and Wi-Fi [26]–[28].

There are three main challenges associated with using SOPs for navigation: (1) the unavailability of appropriate low-level signal models for optimal extraction of states and parameters of interest for navigation and timing purposes, (2) the absence of published receiver architectures capable of producing navigation observables, and (3) the unavailability of error and performance analyses for SOP-based navigation. The first two challenges were addressed in the prequel to this paper for cellular code division multiple access (CDMA) signals. This paper mainly addresses the third challenge by studying a framework for cellular CDMA-based navigation and characterizing the navigation performance for this framework in the presence of sources of errors pertaining to cellular CDMA systems.

Unlike GNSS, the states of a cellular CDMA base transceiver station (BTS) are unknown to a navigating receiver and need to be estimated. Although the cdma200 standard states that a CDMA BTS should transmit its position, local wireless providers do not usually transmit such information [29], [30]. Hence, the positions of the BTSs need to be manually surveyed or estimated on-the-fly individually or collaboratively [31], [32]. A substantial part of the literature on navigation using cellular signals considers time of arrival (TOA) and time difference of arrival (TDOA) measurements; however, certain assumptions such as perfect synchronization or negligible variations between the transmitter and receiver clocks are made to eliminate the clock biases of the BTS and the receiver from the measurement model [33]–[35]. Such assumptions may not hold in practical scenarios; therefore, the receiver and BTS clock biases must be accounted for. While the position states of a BTS are static, the clock error states of the BTS are dynamic and need to be continuously estimated either (1) via a mapping receiver, which shares such estimates with the navigating receiver or (2) by the navigating receiver itself by adopting a simultaneous localization and mapping approach [7], [11], [36]. In either case, the navigating receiver must have appropriate models for (1) the measurement it is drawing from the BTS, (2) relevant BTS states' dynamics, and (3) all relevant sources of errors.

Since SOP-based navigation is a relatively new paradigm, the literature on identification of sources of errors and performance characterization under such errors is scarce for navigation using SOPs. While the performance of cellular CDMA systems has been well studied from a communication systems perspective [37]–[39], the identification of sources of errors that affect

Manuscript received June 28, 2017; revised December 6, 2017; accepted January 17, 2018. Date of publication January 30, 2018; date of current version March 12, 2018. The associate editor coordinating the review of this manuscript and approving it for publication was Dr. Pengfei Xia. This work was supported in part by the Office of Naval Research under Grant N00014-16-1-2305 and in part by a Fellowship from the National Center for Sustainable Transportation, supported by the U.S. Department of Transportation through the University Transportation Centers Program. (Corresponding author: Zaher M. Kassas.)

The authors are with the Department of Electrical and Computer Engineering, University of California, Riverside, Riverside, CA 92521 USA (e-mail: joe.khalife@email.ucr.edu; zkassas@ieee.org).

Color versions of one or more of the figures in this paper are available online at <http://ieeexplore.ieee.org>.

Digital Object Identifier 10.1109/TSP.2018.2799166

the navigation performance of such systems remains a topic of research. In [24], a new source of error pertaining to cellular CDMA systems, namely the discrepancy between the clock biases of different sectors of the same BTS cell, has been discovered. A rudimentary random walk model for the dynamics of the discrepancy was identified and a bound on the optimal estimation performance for a static estimator under such model was derived in [40]. A more elaborate exponentially correlated model for this discrepancy was developed and experimentally validated in the prequel to this paper [41]. This paper derives the optimal estimation performance bounds for the exponentially correlated model for both static and batch estimators. In addition to having appropriate models for these discrepancies, the optimal BTS–receiver geometrical configuration must be identified in order to characterize bounds on the estimation performance. Such configurations have been extensively studied; however, the literature does not provide a lower bound on the estimation error covariance for localization with TOA measurements with non-identical noise variances [42], [43]. This paper also presents the BTS–receiver geometrical configuration that achieves the derived bounds on the estimation performance.

While this paper builds on Part I [41], the contributions herein are comprehensive and independent of its prequel. Part I deals with the identification of the discrepancy between the clock biases of different sectors of the same BTS cell, a practical issue that arises in navigation using cellular CDMA signals, without further analyzing the navigation performance. This paper delves into thorough and rigorous analysis that is not limited to the subjects treated in Part I. To this end, this paper derives theoretical bounds applicable to any set of sensors (receivers) making pseudorange measurements on a source (transmitter). Subsequently, closed-form expressions of these bounds are found in the presence of the discrepancy identified in Part I. This example application is backed with simulation and experimental results. This paper makes three contributions summarized below:

1. Optimal estimation performance with pseudorange measurements:

- A lower bound on the logarithm of the determinant of the estimation error covariance is derived for the case of uncorrelated measurement noise with non-identical variances.
- An optimal BTS–receiver geometrical configuration that achieves the lower bound is identified.
- The above two results are applicable beyond cellular CDMA systems to the general case of a set of sensors (receivers) making pseudorange measurements on a source (transmitter).

2. Optimal estimation performance for the mapper/navigator framework:

- This paper extends the work in [40], presenting a framework for navigating with cellular signals that employs collaborating mapping and navigating receivers. The navigation performance under this framework in the presence of sources of errors pertaining to cellular systems that were identified in [41] is analyzed in this paper. The source of error of interest is namely the discrepancy between the clock bias observed in different sectors of the same BTS cell.

- Lower bounds on the navigation performance of the mapper/navigator framework for static and batch estimators are derived.
- Moreover, a practical upper bound on the position error due to the sector clock bias discrepancy is derived.

3. Experimental results:

- The paper presents experimental results comparing the trajectories corresponding to (1) a navigation solution from GPS and (2) a navigation solution from cellular signals exclusively produced by the cellular CDMA navigation software-defined receiver (SDR) proposed in the prequel paper [41], via the navigation framework discussed in this paper.
- For a ground vehicle, experimental results show a mean distance difference of 5.51 m with a standard deviation of 4.01 m and a maximum difference of 11.11 m.
- For an unmanned aerial vehicle (UAV), experimental results show a reduction in the root-mean square error (RMSE) of 10.57 m with a stationary mapper and 7.04 m with a mobile mapper (another UAV) when the sources of errors are appropriately accounted for using the models derived in Part I of this paper [41].
- In addition, the paper compares the experimental logarithm of the determinant of the estimation error covariance versus the theoretical lower bound derived in this paper.

The remainder of the paper is organized as follows. Section II studies a mapping/navigating receiver framework for navigation with cellular CDMA signals. Section III derives a lower bound on the determinant of the estimation error covariance for pseudorange measurements with uncorrelated measurement noise and analyzes the navigation performance using cellular CDMA signals in the presence of clock bias discrepancies between BTS sectors. Section IV shows experimental results of navigation using cellular CDMA signals for (1) a mobile ground vehicle and stationary mapper, (2) a UAV with a stationary mapper, and (3) a UAV with a mobile mapper. Concluding remarks are provided in Section V.

II. MAPPER/NAVIGATOR FRAMEWORK FOR NAVIGATION WITH CELLULAR CDMA SIGNALS

By making pseudorange observations to 3 or more BTSs, one may estimate the two-dimensional (2-D) position and clock bias of a cellular CDMA receiver, provided that the BTS locations and their clock biases are known. The observability of environments comprising multiple receivers making pseudorange observations on terrestrial SOPs was studied in [9] and the estimation of unknown cellular CDMA SOP states was addressed in [31]. This section describes a framework for navigating with cellular CDMA signals. The framework consists of two receivers: a mapping receiver and a navigating receiver, referred to as the mapper and navigator, respectively [41]. Each receiver is capable of producing pseudorange measurements to nearby SOP BTSs. The mapper could be deployed on top of a building; therefore, it has access to GNSS signals. However, the navigator is located between the buildings where GNSS signals are severely attenuated and cannot be used to produce a navigation

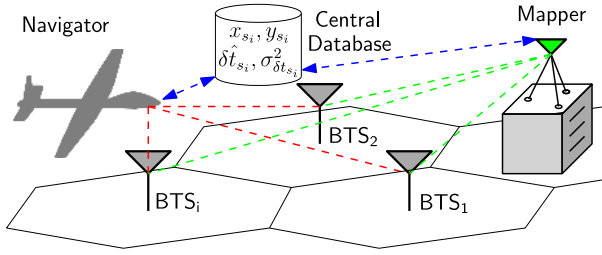


Fig. 1. Mapper and navigator in a cellular SOP environment.

solution. Note that cellular CDMA signals are orders of magnitude more powerful than GNSS signals (carrier-to-noise ratio around 60 dB-Hz, see Fig. 3 in Part I [41], while the carrier-to-noise ratio of GNSS signals outdoors is around 41–46 dB-Hz [44]). Alternatively, the navigator may lose access to GNSS signals in a situation where it is located in the vicinity of a personal privacy device (i.e., GNSS jammer [2]), which makes GNSS signals unusable. Subsequently, the mapper is assumed to have knowledge of its own state vector and is estimating the states of the unknown SOP BTSs. These estimates are shared with the navigator, which has *no* knowledge of its own states. This section considers the estimation of receiver and SOP states in a static framework. As such, the time argument will be dropped for simplicity of notation.

A. Pseudorange Measurement Model

The state of the receiver is defined as $\mathbf{x}_r \triangleq [\mathbf{r}_r^T, c\delta t_r]^T$, where $\mathbf{r}_r = [x_r, y_r]^T$ is the position vector of the receiver, δt_r is the receiver's clock bias, and c is the speed-of-light. Similarly, the state of the i th BTS is defined as $\mathbf{x}_{s_i} \triangleq [\mathbf{r}_{s_i}^T, c\delta t_{s_i}]^T$, where $\mathbf{r}_{s_i} = [x_{s_i}, y_{s_i}]^T$ is the position vector of the i th BTS and δt_{s_i} is the clock bias. The pseudorange measures the time-of-flight of the signal from the BTS to the receiver and can be modeled as the addition of three terms: the true range between the BTS and the receiver, a term due to the difference between the BTS and receiver clock biases, and a measurement noise term [9]. The pseudorange measurement to the i th BTS, ρ_i , can be therefore expressed as

$$\begin{aligned} \rho_i &= \|\mathbf{r}_r - \mathbf{r}_{s_i}\|_2 + c \cdot [\delta t_r - \delta t_{s_i}] + v_i, \\ &\triangleq h_i(\mathbf{x}_r, \mathbf{x}_{s_i}) + v_i, \end{aligned} \quad (1)$$

where $h_i(\mathbf{x}_r, \mathbf{x}_{s_i}) \triangleq \|\mathbf{r}_r - \mathbf{r}_{s_i}\|_2 + c \cdot [\delta t_r - \delta t_{s_i}]$ and v_i is the measurement noise, which is modeled as a zero-mean Gaussian random variable with variance σ_i^2 . Assuming that the receiver is drawing pseudoranges from $N \geq 3$ BTSs with known states, the receiver's state can be estimated by solving a weighted nonlinear least-squares (WNLS) problem [24]. The estimation of the BTS states is discussed next.

B. BTS State Estimation

Consider a mapper with knowledge of its own state vector (by having access to GPS signals, for example) to be present in the navigator's environment as depicted in Fig. 1 [24].

The mapper's objective is to estimate the BTSs' position and clock bias states and share these estimates with the navigator through a central database. The position states of the BTSs are assumed to be known and stored in a database. The position states could be readily obtained via multiple mappers in the environment, estimating the position states of the BTSs for a sufficiently long period of time. These estimates are physically verifiable via surveying or satellite images. Unlike the position state estimates, the clock bias state estimates are time-varying and difficult to verify. Therefore, in the sequel, it is assumed that the mapper is only producing for the i th BTS an estimate $\hat{\delta t}_{s_i}$ and an associated estimation error variance $\sigma_{\delta t_{s_i}}^2$.

Consider M mappers and N SOP BTSs. Denote the state vector of the j th mapper by \mathbf{x}_{r_j} , the pseudorange measurement by the j th mapper on the i th BTS by $\rho_i^{(j)}$, and the corresponding measurement noise by $v_i^{(j)}$. Assume $v_i^{(j)}$ to be independent for all i and j with a corresponding variance $\sigma_i^{(j)2}$. The measurement $\rho_i^{(j)}$ is hence given by

$$\rho_i^{(j)} = \|\mathbf{r}_{r_j} - \mathbf{r}_{s_i}\|_2 + c(\delta t_{r_j} - \delta t_{s_i}) + v_i^{(j)}.$$

The mapper knows \mathbf{r}_{r_j} , \mathbf{r}_{s_i} , and $c\delta t_{r_j}$. Subsequently, define the set of measurements made by all mappers on the i th BTS as

$$\begin{aligned} \mathbf{z}_i &\triangleq \begin{bmatrix} \|\mathbf{r}_{r_1} - \mathbf{r}_{s_i}\| + c\delta t_{r_1} - \rho_i^{(1)} \\ \vdots \\ \|\mathbf{r}_{r_M} - \mathbf{r}_{s_i}\| + c\delta t_{r_M} - \rho_i^{(M)} \end{bmatrix} = \begin{bmatrix} c\delta t_{s_i} - v_i^{(1)} \\ \vdots \\ c\delta t_{s_i} - v_i^{(M)} \end{bmatrix} \\ &= c\delta t_{s_i} \mathbf{1}_M + \mathbf{v}_i, \end{aligned}$$

where $\mathbf{1}_M \triangleq [1, \dots, 1]^T$ and $\mathbf{v}_i \triangleq -[v_i^{(1)}, \dots, v_i^{(M)}]^T$. The clock bias δt_{s_i} is estimated by solving a weighted least-squares (WLS) problem, resulting in the estimate $\hat{\delta t}_{s_i} = \frac{1}{c}(\mathbf{1}_M^T \mathbf{W} \mathbf{1}_M)^{-1} \mathbf{1}_M^T \mathbf{W} \mathbf{z}_i$ and associated estimation error variance $\sigma_{\delta t_{s_i}}^2 = \frac{1}{c}(\mathbf{1}_M^T \mathbf{W} \mathbf{1}_M)^{-1}$, where $\mathbf{W} = \text{diag}[\frac{1}{\sigma_i^{(1)2}}, \dots, \frac{1}{\sigma_i^{(M)2}}]$ is the weighting matrix. The true clock bias of the i th BTS can now be expressed as $\delta t_{s_i} = \hat{\delta t}_{s_i} + w_i$, where w_i is a zero-mean Gaussian random variable with variance $\sigma_{\delta t_{s_i}}^2$.

C. Discrepancy Between Clock Biases of Different Sectors of a BTS

A typical CDMA BTS transmits into three different sectors within a particular cell. Ideally, all sectors' clocks should be driven by the same oscillator, which implies that the same clock bias (after correcting for the pseudo noise sequence offset) should be observed in all sectors of the same cell. However, factors such as unknown distance between the phase-center of the sector antennas, delays due to RF connectors and other components (e.g., cabling, filters, amplifiers, etc.) cause the clock biases corresponding to different BTS sectors to be slightly different. This behavior was consistently observed experimentally at different times and different BTS locations corresponding to different cellular providers [45]. A sample realization of the observed clock bias for different BTS sectors is depicted in Fig. 2.

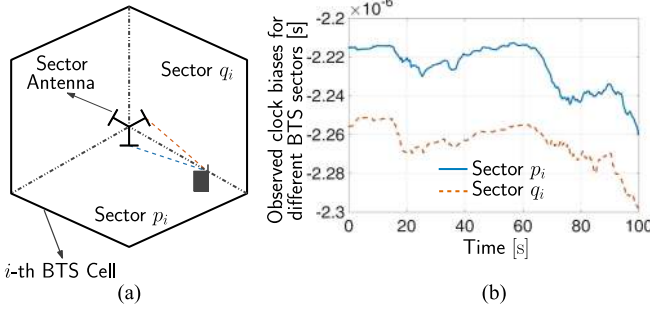


Fig. 2. (a) A receiver placed at the border of two sectors of a cell, making pseudorange observations on both sector antennas simultaneously. The receiver has knowledge of its own states (from GPS signals) and has knowledge of the BTS position states. (b) Observed BTS clock bias for the two sectors (after correcting for the pseudo noise sequence offset).

The clock biases observed in sectors p_i and q_i of the i th BTS are denoted by $\delta t_{s_i}^{(p_i)}$ and $\delta t_{s_i}^{(q_i)}$, respectively. The relationship between $\delta t_{s_i}^{(p_i)}$ and $\delta t_{s_i}^{(q_i)}$ is captured by

$$\delta t_{s_i}^{(q_i)} = \delta t_{s_i}^{(p_i)} + [1 - 1_{q_i}(p_i)] \cdot \epsilon_i,$$

where ϵ_i is a random sequence that models the discrepancy between the sectors' clock biases and

$$1_{q_i}(p_i) = \begin{cases} 1, & \text{if } p_i = q_i, \\ 0, & \text{otherwise,} \end{cases}$$

is the indicator function. A model for the discrepancy ϵ_i was identified in [41], which is given by

$$\epsilon_i(k) = \phi_i^k \epsilon_i(0) + \sum_{l=0}^{k-1} \phi_i^{k-1-l} \zeta_i(l),$$

where $\phi_i \triangleq e^{-\alpha_i T}$, α_i is the inverse of the system's time constant (on the order of 10^{-4} Hz), ζ_i is a zero-mean Laplace-distributed random sequence with parameter λ_i (in continuous-time), and k is the time index. The initial discrepancy $\epsilon_i(0)$ is assumed to be known and without loss of generality, is assumed to be zero. After nine time steps, ϵ_i can be modeled as a zero-mean Gaussian random variable with variance $\frac{\lambda_i^2}{\alpha_i} (1 - e^{-2\alpha_i k T})$ [41]. In the sequel, $\lambda_i \equiv \lambda$ and $\alpha_i \equiv \alpha$, $\forall i$. The discrepancy ϵ_i can be particularly harmful if the mapper and navigator are listening to two different sectors of the same BTS cell. The resulting pseudorange model in the presence of this discrepancy is presented in the next subsection.

D. Pseudorange Model in the Presence of Sector Mismatch

Since the navigator is using the BTS clock bias estimate produced by the mapper(s), the pseudorange measured by the navigator in sector q_i of the i th BTS can be expressed as

$$\rho_i^{(q_i)} = \hat{h}_i^{(p_i)} + \eta_i - [1 - 1_{q_i}(p_i)] \cdot [c\epsilon_i],$$

where $\hat{h}_i^{(p_i)} \triangleq h_i(\mathbf{x}_r, \hat{\mathbf{x}}_{s_i}^{(p_i)})$, $\hat{\mathbf{x}}_{s_i}^{(p_i)} = [\mathbf{r}_{s_i}^T, c\delta t_{s_i}^{(p_i)}]^T$, $\delta t_{s_i}^{(p_i)}$ is the i th BTS clock bias estimate produced by the mapper in sector p_i , and $\eta_i \triangleq v_i - w_i$ models the overall uncertainty in the pseudorange measurement, which is a zero-mean Gaussian

random variable with variance $\sigma_{\eta_i}^2 = \sigma_v^2 + c^2 \sigma_{\delta t_{s_i}}^2$. The quantities ϵ_i , η_i , and $\delta t_{s_i}^{(p_i)}$ are time-varying quantities with $\delta t_{s_i}^{(p_i)}$ known at all times. Therefore, the pseudorange at time-step k is given by

$$\rho_i^{(q_i)}(k) = \hat{h}_i^{(p_i)}(k) + \eta_i(k) - [1 - 1_{q_i}(p_i)] \cdot [c\epsilon_i(k)], \quad (2)$$

where $\hat{h}_i^{(p_i)}(k) = h_i[\mathbf{x}_r(k), \hat{\mathbf{x}}_{s_i}^{(p_i)}(k)]$ indicates that the observation estimate is calculated using the mapper estimates and the receiver state at time k .

E. Fusion of BTS Clock State Estimates Into the Navigation Solution

The navigator is assumed to be drawing pseudorange measurements from N BTSs, N_s of which have a mismatch between the mapper and navigator sectors. Without loss of generality, the set of pseudorange measurements are assumed to be sorted such that the first N_s measurements correspond to ones coming from the BTSs with sector mismatch between the mapper and navigator. If the navigator is either stationary or mobile but has perfect knowledge of the change in its position, it can solve through a batch LS estimator for its: (1) initial position state $\mathbf{r}_r(k_0)$ and (2) clock bias at time-steps k_0 to $k_0 + K - 1$ by utilizing all the measurements from k_0 to $k_0 + K - 1$. Alternatively, the navigator may solve for its current position and clock bias through a LS estimator (point solution with $K = 1$). In either case, the estimator is estimating the state vector \mathbf{x}'_r given by

$$\mathbf{x}'_r = [x_r(k_0), y_r(k_0), c\delta t_r(k_0), \dots, c\delta t_r(k_0 + K - 1)]^T.$$

The measurement model is therefore given by

$$\boldsymbol{\rho} = \hat{\mathbf{h}} + c\boldsymbol{\epsilon} + \boldsymbol{\eta}, \quad (3)$$

where

$$\boldsymbol{\rho} \triangleq [\rho_1^T, \dots, \rho_N^T]^T,$$

$${}^K \boldsymbol{\rho}_i \triangleq [\rho_i^{(q_i)}(k_0), \dots, \rho_i^{(q_i)}(k_0 + K - 1)]^T,$$

$$\hat{\mathbf{h}} \triangleq [\hat{h}_1^T, \dots, \hat{h}_N^T]^T,$$

$${}^K \hat{\mathbf{h}}_i \triangleq [\hat{h}_i^{(p_i)}(k_0), \dots, \hat{h}_i^{(p_i)}(k_0 + K - 1)]^T,$$

$$\boldsymbol{\epsilon} \triangleq [\epsilon_1^T, \dots, \epsilon_N^T, \mathbf{0}_{K \times 1}]^T,$$

$${}^K \boldsymbol{\epsilon}_i \triangleq [\epsilon_i(k_0), \dots, \epsilon_i(k_0 + K - 1)]^T,$$

$$\boldsymbol{\eta} \triangleq [\eta_1^T, \dots, \eta_N^T]^T, \quad {}^K \boldsymbol{\eta}_i \triangleq [\eta_i(k_0), \dots, \eta_i(k_0 + K - 1)]^T,$$

and $\bar{K} \triangleq K \cdot (N - N_s)$. The Jacobian matrix \mathbf{H} of the set of observations with respect to \mathbf{x}'_r is given by $\mathbf{H} = [\mathbf{G} \ \bar{\mathbf{I}}_N]$, where $\mathbf{G} \triangleq [\frac{\mathbf{r}_r - \mathbf{r}_{s_1}}{\|\mathbf{r}_r - \mathbf{r}_{s_1}\|} \mathbf{1}_K^T \ \dots \ \frac{\mathbf{r}_r - \mathbf{r}_{s_N}}{\|\mathbf{r}_r - \mathbf{r}_{s_N}\|} \mathbf{1}_K^T]$ and $\bar{\mathbf{I}}_N \triangleq [\mathbf{I}_{K \times K} \ \dots \ \mathbf{I}_{K \times K}]^T$ where $\mathbf{I}_{K \times K}$ indicates the $K \times K$ identity matrix. The "overall" measurement noise, $(c\boldsymbol{\epsilon} + \boldsymbol{\eta})$, captures the errors due to measurement noise, mapper estimation errors,

and discrepancies between the sectors' clock biases. It is modeled as a zero-mean random variable with a covariance matrix \mathbf{R} . The structure of \mathbf{R} will be discussed in Subsections III-B–III-C. The navigator's state can now be estimated by solving a WNLS problem, to obtain an estimate of its state $\hat{\mathbf{x}}'_r$ and an associated estimation error covariance \mathbf{P} . The iterated WNLS equations are given by

$$\begin{aligned}\hat{\mathbf{x}}'_r{}^{(l+1)} &= \hat{\mathbf{x}}'_r{}^{(l)} + (\mathbf{H}^T \mathbf{R}^{-1} \mathbf{H})^{-1} \mathbf{H}^T \mathbf{R}^{-1} (\boldsymbol{\rho} - \hat{\boldsymbol{\rho}}) \\ \mathbf{P}^{(l)} &= (\mathbf{H}^T \mathbf{R}^{-1} \mathbf{H})^{-1},\end{aligned}$$

where l is the iteration number and $\hat{\boldsymbol{\rho}} \triangleq \hat{\mathbf{h}}$ evaluated at the current estimate $\hat{\mathbf{x}}'_r{}^{(l)}$.

III. PERFORMANCE CHARACTERIZATION IN THE PRESENCE OF SECTOR CLOCK BIAS DISCREPANCIES

In this section, the estimation performance in the presence of the discrepancy discussed in Subsection II-C is analyzed as a function of time and the number of mismatches between the BTS cell sectors which the mappers are listening to and those cell sectors which the navigator is listening to. The estimation performance was characterized for a special case of this problem and for a static estimator only, where the discrepancy model was assumed to adhere to a random walk [40]. This section derives lower bounds on the determinant of the estimation error covariance for point and batch estimators with uncorrelated measurements between sets of sensors (SOPs), where each set has an arbitrary measurement noise covariance, and for a discrepancy that is modeled as an exponentially correlated random sequence. First, a general lower bound on the determinant of the estimation error covariance in the case of uncorrelated measurement noise is derived. Next, analytical expressions of the lower bounds on the determinant of the estimation error covariance in the presence of sector mismatch for two estimation frameworks are presented, namely a point solution and a batch solution. Finally, a practical upper bound on the position error is derived.

A. Estimation Error Covariance Lower Bound

This subsection derives the lower bound on the determinant of the estimation error covariance (D-optimality criterion) in the case of uncorrelated measurement noise and specifies an optimal BTS configuration that achieves this bound. The D-optimality criterion is chosen, since it is equivalent to minimizing the volume of the uncertainty ellipsoid [46] and is also a commonly used metric when studying the geometric dilution of precision [47]. The results are captured in the following two theorems. It is important to note that the results presented in these two theorems are applicable beyond cellular CDMA systems. In fact, they apply to the general problem of a set of sensors (receiver) making pseudorange measurements on a source (transmitter). This problem is encountered in navigation and source localization.

Theorem III.1: Given $N \geq 3$ sets of K pseudorange measurements modeled according to (3) with a measurement noise covariance $\mathbf{R} = \text{diag}[\mathbf{R}_1, \dots, \mathbf{R}_N]$ where $\{\mathbf{R}_i\}_{i=1}^N$ is a set of $K \times K$ positive definite matrices, the determinant of the

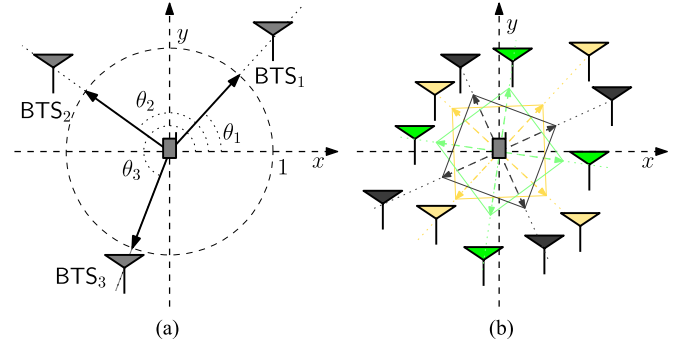


Fig. 3. (a) Re-parametrization of the unit line-of-sight (LOS) vectors by the bearing angles. (b) Optimal distribution of the BTSs around the receiver where each color represents a different set of BTSs.

estimation error covariance \mathbf{P} is lower bounded by

$$\det[\mathbf{P}] \geq \frac{4}{\left(\sum_{i=1}^N \mathbf{1}_K^T \mathbf{R}_i^{-1} \mathbf{1}_K\right)^2 \det\left[\sum_{i=1}^N \mathbf{R}_i^{-1}\right]}. \quad (4)$$

Proof: First, the Jacobian matrix \mathbf{H} is re-parameterized by the bearing angles $\{\theta_i\}_{i=1}^N$ between the receiver and the N BTSs, as shown in Fig. 3(a). Subsequently, the matrix \mathbf{G} can be re-expressed as $\mathbf{G} = [\mathbf{x} \ \mathbf{y}]$, where $\mathbf{x} \triangleq [\cos \theta_1 \mathbf{1}_K^T, \dots, \cos \theta_N \mathbf{1}_K^T]$ and $\mathbf{y} \triangleq [\sin \theta_1 \mathbf{1}_K^T, \dots, \sin \theta_N \mathbf{1}_K^T]$. The information matrix \mathbf{M} is given by

$$\mathbf{M} = \mathbf{P}^{-1} = \mathbf{H}^T \mathbf{R}^{-1} \mathbf{H} = \begin{bmatrix} \mathbf{G}^T \mathbf{R}^{-1} \mathbf{G} & \mathbf{G}^T \mathbf{R}^{-1} \bar{\mathbf{I}}_N \\ \bar{\mathbf{I}}_N^T \mathbf{R}^{-1} \mathbf{G} & \bar{\mathbf{I}}_N^T \mathbf{R}^{-1} \bar{\mathbf{I}}_N \end{bmatrix}.$$

Assuming that \mathbf{G} is full column-rank, which is guaranteed whenever at least three of the BTSs are non-collinear, and from the Schur complement properties, the determinant of \mathbf{M} can be expressed as

$$\det[\mathbf{M}] = \det[\mathbf{M}_1] \det[\mathbf{M}_2 - \mathbf{M}_3],$$

where $\mathbf{M}_1 \triangleq \mathbf{G}^T \mathbf{R}^{-1} \mathbf{G}$, $\mathbf{M}_2 \triangleq \bar{\mathbf{I}}_N^T \mathbf{R}^{-1} \bar{\mathbf{I}}_N = \sum_{i=1}^N \mathbf{R}_i^{-1}$, and $\mathbf{M}_3 \triangleq \bar{\mathbf{I}}_N^T \mathbf{R}^{-1} \mathbf{G} (\mathbf{G}^T \mathbf{R}^{-1} \mathbf{G})^{-1} \mathbf{G}^T \mathbf{R}^{-1} \bar{\mathbf{I}}_N$. By definition, \mathbf{M} is a positive definite matrix, hence

$$\mathbf{M}_1 \succ \mathbf{0} \quad \text{and} \quad \mathbf{M}_2 - \mathbf{M}_3 \succ \mathbf{0}.$$

Also by definition, \mathbf{M}_2 is a positive definite matrix. Since \mathbf{G} is full column-rank and \mathbf{R}^{-1} is positive-definite, then $(\mathbf{G}^T \mathbf{R}^{-1} \mathbf{G})^{-1}$ will be positive-definite as well. The matrix \mathbf{M}_3 may also be expressed as $\mathbf{M}_3 = \mathbf{B}^T (\mathbf{G}^T \mathbf{R}^{-1} \mathbf{G})^{-1} \mathbf{B}$, where $\mathbf{B} \triangleq \mathbf{G}^T \mathbf{R}^{-1} \bar{\mathbf{I}}_N$; which readily shows that \mathbf{M}_3 is positive semi-definite. Therefore, it can be deduced that

$$\mathbf{M}_2 \succeq \mathbf{M}_2 - \mathbf{M}_3,$$

and hence

$$\det[\mathbf{M}_2] \geq \det[\mathbf{M}_2 - \mathbf{M}_3].$$

Subsequently, the following upper bound may be established on $\det[\mathbf{M}]$

$$\det[\mathbf{M}] \leq \det[\mathbf{G}^T \mathbf{R}^{-1} \mathbf{G}] \det\left[\sum_{i=1}^N \mathbf{R}_i^{-1}\right]. \quad (5)$$

The matrix $\mathbf{M}_1 = \mathbf{G}^\top \mathbf{R}^{-1} \mathbf{G}$ may be expressed as

$$\mathbf{G}^\top \mathbf{R}^{-1} \mathbf{G} = \begin{bmatrix} \mathbf{x}^\top \mathbf{R}^{-1} \mathbf{x} & \mathbf{x}^\top \mathbf{R}^{-1} \mathbf{y} \\ \mathbf{y}^\top \mathbf{R}^{-1} \mathbf{x} & \mathbf{y}^\top \mathbf{R}^{-1} \mathbf{y} \end{bmatrix},$$

which has the determinant

$$\det[\mathbf{G}^\top \mathbf{R}^{-1} \mathbf{G}] = (\mathbf{x}^\top \mathbf{R}^{-1} \mathbf{x})(\mathbf{y}^\top \mathbf{R}^{-1} \mathbf{y}) - (\mathbf{x}^\top \mathbf{R}^{-1} \mathbf{y})^2 \leq (\mathbf{x}^\top \mathbf{R}^{-1} \mathbf{x})(\mathbf{y}^\top \mathbf{R}^{-1} \mathbf{y}). \quad (6)$$

Equations (5) and (6) yield

$$\det[\mathbf{M}] \leq (\mathbf{x}^\top \mathbf{R}^{-1} \mathbf{x})(\mathbf{y}^\top \mathbf{R}^{-1} \mathbf{y}) \det\left[\sum_{i=1}^N \mathbf{R}_i^{-1}\right]. \quad (7)$$

Using the definition of \mathbf{x} and \mathbf{y} and noting that $\mathbf{R}^{-1} = \text{diag}[\mathbf{R}_1^{-1}, \dots, \mathbf{R}_N^{-1}]$, the following can be deduced

$$\begin{aligned} \mathbf{x}^\top \mathbf{R}^{-1} \mathbf{x} + \mathbf{y}^\top \mathbf{R}^{-1} \mathbf{y} &= \sum_{i=1}^N \mathbf{1}_K^\top \mathbf{R}_i^{-1} \mathbf{1}_K \cos^2 \theta_i \\ &\quad + \sum_{i=1}^N \mathbf{1}_K^\top \mathbf{R}_i^{-1} \mathbf{1}_K \sin^2 \theta_i \\ &= \sum_{i=1}^N \mathbf{1}_K^\top \mathbf{R}_i^{-1} \mathbf{1}_K. \end{aligned} \quad (8)$$

Defining $u \triangleq \mathbf{x}^\top \mathbf{R}^{-1} \mathbf{x}$ and $a \triangleq \sum_{i=1}^N \mathbf{1}_K^\top \mathbf{R}_i^{-1} \mathbf{1}_K$ and incorporating the geometric constraint (8) into (7) yields

$$\det[\mathbf{M}] \leq u(a - u) \det\left[\sum_{i=1}^N \mathbf{R}_i^{-1}\right]. \quad (9)$$

The right-hand side of (9) is maximized when $u^* = \frac{a}{2} = \frac{1}{2} \sum_{i=1}^N \mathbf{1}_K^\top \mathbf{R}_i^{-1} \mathbf{1}_K$. This finally yields

$$\det[\mathbf{P}] = \frac{1}{\det[\mathbf{M}]} \geq \frac{4}{\left(\sum_{i=1}^N \mathbf{1}_K^\top \mathbf{R}_i^{-1} \mathbf{1}_K\right)^2 \det\left[\sum_{i=1}^N \mathbf{R}_i^{-1}\right]}.$$

Corollary III.1.1: If $K = 1$, i.e., $\mathbf{R}_i = \sigma_i^2$, the lower bound simplifies to

$$\det[\mathbf{P}] \geq \frac{4}{[\text{trace}(\mathbf{R}^{-1})]^3}.$$

Proof: This can be seen by noting that $\sum_{i=1}^N \mathbf{1}_K^\top \mathbf{R}_i^{-1} \mathbf{1}_K = \sum_{i=1}^N \mathbf{R}_i^{-1} = \sum_{i=1}^N \frac{1}{\sigma_i^2} = \text{trace}(\mathbf{R}^{-1})$. ■

Theorem III.2: Given a total of N BTSs grouped into L sets with $N_l \geq 3$ BTSs in each set, where $l = 1, \dots, L$, and given that the receiver is drawing K pseudorange measurements from each set of BTSs with noise covariance $\{\Sigma_l = \text{diag}[\mathbf{R}_l, \dots, \mathbf{R}_l]\}_{l=1}^L$ where $\{\mathbf{R}_l\}_{l=1}^L$ is a set of $K \times K$ positive definite matrices, the optimal estimation performance that minimizes the determinant of the estimation error covariance is achieved when each set of BTSs forms a regular polygon around the receiver, i.e.,

$$\theta_{i_l}^{(l)} = \frac{2\pi}{N_l} i_l + \theta_0^{(l)}, \quad i_l = 1, \dots, N_l,$$

where $\theta_{i_l}^{(l)}$ is the bearing angle between the receiver and the i_l th BTS in l th set and $\theta_0^{(l)}$ is an arbitrary offset angle.

The optimal BTS configuration is illustrated in Fig. 3(b).

Proof: In general, for $\{\theta_{i_l} = \frac{2\pi i_l}{N_l} + \theta_{i_0}\}_{i_l=1}^{N_l}$ and any integer $N_l \geq 3$ and constant offset angle θ_{i_0} , the following holds [48]

$$\sum_{i_l=1}^{N_l} \cos^2 \theta_{i_l} = \sum_{i_l=1}^{N_l} \sin^2 \theta_{i_l} = \frac{N_l}{2}, \quad (10)$$

$$\sum_{i_l=1}^{N_l} \cos \theta_{i_l} \sin \theta_{i_l} = \sum_{i_l=1}^{N_l} \cos \theta_{i_l} = \sum_{i_l=1}^{N_l} \sin \theta_{i_l} = 0. \quad (11)$$

Note that (10) and (11) hold for any offset angle θ_{i_0} . The information matrix can be expressed as

$$\mathbf{M} = \begin{bmatrix} \mathbf{x}^\top \mathbf{R}^{-1} \mathbf{x} & \mathbf{x}^\top \mathbf{R}^{-1} \mathbf{y} & \mathbf{x}^\top \mathbf{R}^{-1} \bar{\mathbf{I}}_N \\ \mathbf{y}^\top \mathbf{R}^{-1} \mathbf{x} & \mathbf{y}^\top \mathbf{R}^{-1} \mathbf{y} & \mathbf{y}^\top \mathbf{R}^{-1} \bar{\mathbf{I}}_N \\ \bar{\mathbf{I}}_N^\top \mathbf{R}^{-1} \mathbf{x} & \bar{\mathbf{I}}_N^\top \mathbf{R}^{-1} \mathbf{y} & \bar{\mathbf{I}}_N^\top \mathbf{R}^{-1} \bar{\mathbf{I}}_N \end{bmatrix}.$$

Define the partitioned vectors

$$\mathbf{x} \triangleq \begin{bmatrix} \mathbf{x}_1 \\ \vdots \\ \mathbf{x}_L \end{bmatrix}, \quad \mathbf{y} \triangleq \begin{bmatrix} \mathbf{y}_1 \\ \vdots \\ \mathbf{y}_L \end{bmatrix}, \quad \mathbf{1}_N \triangleq \begin{bmatrix} \mathbf{1}_{N_1} \\ \vdots \\ \mathbf{1}_{N_L} \end{bmatrix},$$

where $\mathbf{x}_l = [\cos \theta_1^{(l)} \mathbf{1}_K^\top, \dots, \cos \theta_{N_l}^{(l)} \mathbf{1}_K^\top]^\top$ and $\mathbf{y}_l = [\sin \theta_1^{(l)} \mathbf{1}_K^\top, \dots, \sin \theta_{N_l}^{(l)} \mathbf{1}_K^\top]^\top$, where $l = 1, \dots, L$. The overall measurement noise covariance is defined as

$$\mathbf{R} \triangleq \text{diag}[\Sigma_1, \dots, \Sigma_L],$$

where $\Sigma_l = \text{diag}[\mathbf{R}_l, \dots, \mathbf{R}_l]$ (repeated N_l times). Subsequently, $\mathbf{x}^\top \mathbf{R}^{-1} \mathbf{x}$ can be expressed as

$$\begin{aligned} \mathbf{x}^\top \mathbf{R}^{-1} \mathbf{x} &= \sum_{l=1}^L \mathbf{x}_l^\top \Sigma_l^{-1} \mathbf{x}_l \\ &= \sum_{l=1}^L \sum_{i_l=1}^{N_l} \mathbf{1}_K^\top \mathbf{R}_l^{-1} \mathbf{1}_K \cos^2 \theta_{i_l}^{(l)} \\ &= \sum_{l=1}^L \mathbf{1}_K^\top \mathbf{R}_l^{-1} \mathbf{1}_K \sum_{i_l=1}^{N_l} \cos^2 \theta_{i_l}^{(l)}. \end{aligned} \quad (12)$$

Similarly, it can be shown that

$$\mathbf{x}^\top \mathbf{R}^{-1} \mathbf{x} = \sum_{l=1}^L \mathbf{1}_K^\top \mathbf{R}_l^{-1} \mathbf{1}_K \sum_{i_l=1}^{N_l} \sin^2 \theta_{i_l}^{(l)}, \quad (13)$$

$$\mathbf{x}^\top \mathbf{R}^{-1} \mathbf{y} = \sum_{l=1}^L \mathbf{1}_K^\top \mathbf{R}_l^{-1} \mathbf{1}_K \sum_{i_l=1}^{N_l} \cos \theta_{i_l}^{(l)} \sin \theta_{i_l}^{(l)}, \quad (14)$$

$$\mathbf{x}^\top \mathbf{R}^{-1} \bar{\mathbf{I}}_N = \sum_{l=1}^L \mathbf{1}_K^\top \mathbf{R}_l^{-1} \sum_{i_l=1}^{N_l} \cos \theta_{i_l}^{(l)}, \quad (15)$$

$$\mathbf{y}^T \mathbf{R}^{-1} \bar{\mathbf{I}}_N = \sum_{l=1}^L \mathbf{1}_K^T \mathbf{R}_l^{-1} \sum_{i_l=1}^{N_l} \sin \theta_{i_l}^{(l)}, \quad (16)$$

$$\bar{\mathbf{I}}_N^T \mathbf{R}^{-1} \bar{\mathbf{I}}_N = \sum_{l=1}^L N_l \mathbf{R}_l^{-1}. \quad (17)$$

From (10)–(17) and the optimal BTS configuration, i.e., each set of BTSs forms a regular polygon around the receiver, the information matrix can be expressed as,

$$\mathbf{M} = \begin{bmatrix} \sum_{l=1}^L \frac{N_l}{2} \mathbf{1}_K^T \mathbf{R}_l^{-1} \mathbf{1}_K & 0 & \mathbf{0}_{K \times 1}^T \\ 0 & \sum_{l=1}^L \frac{N_l}{2} \mathbf{1}_K^T \mathbf{R}_l^{-1} \mathbf{1}_K & \mathbf{0}_{K \times 1}^T \\ \mathbf{0}_{K \times 1} & \mathbf{0}_{K \times 1} & \sum_{l=1}^L N_l \mathbf{R}_l^{-1} \end{bmatrix},$$

hence

$$\mathbf{P} = \begin{bmatrix} \frac{2}{\sum_{l=1}^L N_l \mathbf{1}_K^T \mathbf{R}_l^{-1} \mathbf{1}_K} & 0 & \mathbf{0}_{K \times 1}^T \\ 0 & \frac{2}{\sum_{l=1}^L N_l \mathbf{1}_K^T \mathbf{R}_l^{-1} \mathbf{1}_K} & \mathbf{0}_{K \times 1}^T \\ \mathbf{0}_{K \times 1} & \mathbf{0}_{K \times 1} & \left[\sum_{l=1}^L N_l \mathbf{R}_l^{-1} \right]^{-1} \end{bmatrix}. \quad (18)$$

By noting that $\sum_{i=1}^N \mathbf{1}_K^T \mathbf{R}_i^{-1} \mathbf{1}_K = \sum_{l=1}^L N_l \mathbf{1}_K^T \mathbf{R}_l^{-1} \mathbf{1}_K$ and that $\sum_{i=1}^N \mathbf{R}_i^{-1} = \sum_{l=1}^L N_l \mathbf{R}_l^{-1}$, the determinant of the estimation error covariance may be expressed as

$$\det[\mathbf{P}] = \frac{4}{\left(\sum_{i=1}^N \mathbf{1}_K^T \mathbf{R}_i^{-1} \mathbf{1}_K \right)^2 \det \left[\sum_{i=1}^N \mathbf{R}_i^{-1} \right]}. \quad (19)$$

Therefore, the configuration described in Theorem III.2 (with determinant computed in (19)) indeed achieves the lower bound established in Theorem III.1 (cf. (4)). ■

It is worth noting that the results in Theorem III.2 are applicable beyond cellular CDMA systems and the mapper/navigator framework. The problem can be regarded as an optimal sensor placement problem, where it is desired to place sensors (mappers) in a way that minimizes the uncertainty in the SOP's state. Moreover, these results can provide an insight on the minimum requirements of the system. If the required performance happens to violate the bound, the system designer will know that this performance is not achievable and either more SOPs or sensors must be employed or more measurements must be taken. Hence, Theorem III.2 could be used to deduce necessary system settings to make a desired performance achievable. The optimal performance based on minimizing the determinant of the estimation error covariance in the presence of sector mismatch is analyzed next.

B. Lower Bound on the Determinant of the Estimation Error Covariance in the Presence of Sector Mismatch: Point Solution

In this scenario, the navigator is solving for its state at time k using the measurements made at time k , i.e., $k_0 = k$ and $K = 1$. The overall measurement noise covariance in this case is given by

$$\mathbf{R} = \text{diag} \left[(\sigma_\eta^2 + \sigma_\epsilon^2(k)) \mathbf{I}_{N_s \times N_s}, \sigma_\eta^2 \mathbf{I}_{(N-N_s) \times (N-N_s)} \right], \quad (20)$$

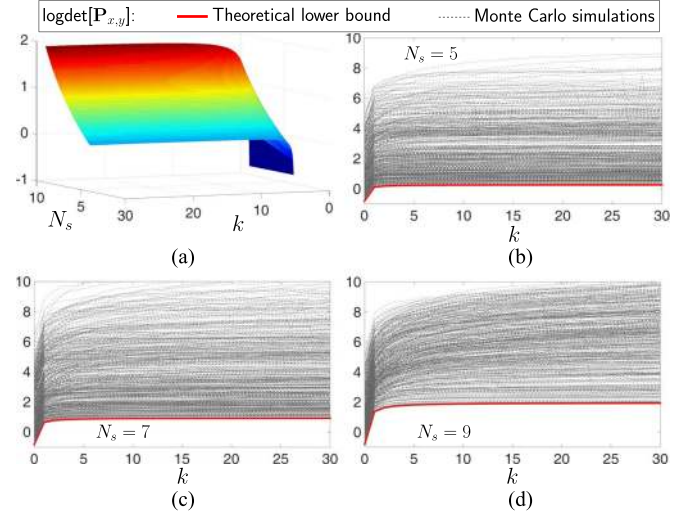


Fig. 4. (a) Surface plot of $\log \det[\mathbf{P}_{x,y}^*]$ as a function of N_s and k . (b)–(d) Plots of $\log \det[\mathbf{P}_{x,y}]$ for 500 Monte Carlo simulations along with the theoretical lower bound $\log \det[\mathbf{P}_{x,y}^*]$. Simulation parameters: $N = 12$, $T = 0.2\text{s}$, $\alpha = 10^{-3}\text{Hz}$, $\sigma_\eta^2 = 4\text{m}^2$, and $\lambda = 66\text{ns/s}$.

where $\sigma_\epsilon^2(k) \triangleq \frac{c^2 \lambda^2}{\alpha} (1 - e^{-2\alpha k T})$. By applying Theorem III.2 and Corollary III.1.1, the optimal estimation error covariance under sector clock bias discrepancies can be found from (18) to yield

$$\mathbf{P}^* = \begin{bmatrix} \mathbf{P}_{x,y}^* & \mathbf{0}_{2 \times 1} \\ \mathbf{0}_{1 \times 2} & (\sigma_{c\delta t_r}^*)^2 \end{bmatrix} = \begin{bmatrix} 2\sigma_{\text{eq}}^2 \mathbf{I}_{2 \times 2} & \mathbf{0}_{2 \times 1} \\ \mathbf{0}_{1 \times 2} & \sigma_{\text{eq}}^2 \end{bmatrix}, \quad (21)$$

where

$$\begin{aligned} \sigma_{\text{eq}}^2 &\triangleq \frac{1}{\text{trace}(\mathbf{R}^{-1})} = \frac{1}{\frac{N_s}{\sigma_\eta^2 + \sigma_\epsilon^2(k)} + \frac{N-N_s}{\sigma_\eta^2}} \\ &= \frac{\left[\sigma_\eta^2 + \frac{c^2 \lambda^2}{\alpha} (1 - e^{-2\alpha k T}) \right] \sigma_\eta^2}{N \sigma_\eta^2 + (N - N_s) \frac{c^2 \lambda^2}{\alpha} (1 - e^{-2\alpha k T})}. \end{aligned} \quad (22)$$

In order to demonstrate the result in (21), Monte Carlo simulations were conducted for several N_s and k values. The logarithm of the determinant of each resulting position estimation error covariance $\mathbf{P}_{x,y}$, namely $\log \det[\mathbf{P}_{x,y}]$, for 500 runs were plotted along with $\log \det[\mathbf{P}_{x,y}^*]$ obtained in (21). A surface plot of $\log \det[\mathbf{P}_{x,y}^*]$ and the Monte Carlo simulation results for $\log \det[\mathbf{P}_{x,y}]$ are shown in Fig. 4.

The following remarks can be concluded from these simulations.

Remark 1: For a fixed $N_s < N$, $\log \det[\mathbf{P}_{x,y}^*]$ becomes almost constant after five to ten time steps and converges to a constant value that can be approximated to be

$$\lim_{k \rightarrow \infty} \log \det[\mathbf{P}_{x,y}^*] \approx \log \left[4 \left(\frac{\sigma_\eta^2}{N - N_s} \right)^2 \right]. \quad (23)$$

The derivation of (23) is given in Appendix A. The same expression is obtained when the navigator uses only the measurements from the $N - N_s$ BTSs with no sector mismatch to estimate its state. This is attributed to the fact that the variance of the error in the measurements coming from the BTSs with sector

mismatch increases with time until it reaches a steady value (cf. (20)). This steady state value is much larger than σ_η^2 and therefore these measurements will be “almost neglected” by the estimator.

Remark 2: For large k , one can approximate $\log \det[\mathbf{P}_{x,y}^*]$

$$\log \det [\mathbf{P}_{x,y}^*] \approx -2 \log \left(1 - \frac{N_s}{N} \right) + \xi, \quad (24)$$

where ξ is a finite constant. The derivation of (24) is given in Appendix B. It can be readily seen that (24) approaches ∞ as N_s approaches N . It is therefore imperative to have at least one BTS with no sector mismatch in order for the estimation error covariance to be bounded.

C. Lower Bound on the Determinant of the Estimation Error Covariance in the Presence of Sector Mismatch: Batch Estimator

In this scenario, the navigator is assumed to be either stationary or mobile but has perfect knowledge of the change in its position with $k_0 = 1$ and $K > 1$. Starting at $k_0 = 1$ ensures that the pseudorange measurements are affected by the error due to clock bias discrepancy in the case of sector mismatch. In order to make the analysis more tractable, the exponentially correlated model in the batch estimator is approximated by a random walk, i.e., $\alpha \rightarrow 0$. For small values of α and k , the relative error between the variances of these processes is guaranteed to be less than an arbitrary small threshold [41]. Subsequently, $\sigma_\epsilon^2(k)$ is approximated by

$$\sigma_\epsilon^2(k) \approx \bar{\sigma}_\epsilon^2(k) \triangleq \lim_{\alpha \rightarrow 0} \sigma_\epsilon^2(k) = 2kTc^2\lambda^2, \quad (25)$$

where $k = 1, \dots, K$. The overall measurement noise covariance in this case is given by

$$\mathbf{R} = \text{diag} [\mathbf{R}_1, \dots, \mathbf{R}_N],$$

where $\{\mathbf{R}_i\}_{i=1}^N$ is a set of $K \times K$ positive definite matrices with

$$\mathbf{R}_i = \begin{cases} \sigma_\eta^2 \mathbf{I}_{K \times K} + \mathbf{R}_\epsilon, & \text{if } i \leq N_s, \\ \sigma_\eta^2 \mathbf{I}_{K \times K}, & \text{otherwise,} \end{cases}$$

where

$$[\mathbf{R}_\epsilon]_{m,n} = \sigma_\epsilon^2 [\min \{m, n\}], \quad m, n = 1, \dots, K,$$

and $[\Psi]_{m,n}$ denotes the element in the m th row and n th column of matrix Ψ . Using this approximation of $\sigma_{\eta_s}^2(k)$ and by applying Theorem III.2, the optimal estimation error covariance under sector clock bias discrepancies for a batch estimator can be approximated by

$$\mathbf{P}^{f*} \approx \begin{bmatrix} \mathbf{P}_{x,y}^{f*} & \mathbf{0}_{K \times 1}^T \\ \mathbf{0}_{K \times 1} & \mathbf{P}_{c\delta t_r}^{f*} \end{bmatrix},$$

where

$$\mathbf{P}_{x,y}^{f*} = \frac{4c^2\lambda^2T\sigma_\eta^2\mathbf{I}_{2 \times 2}}{f(\beta)\sigma_\eta^2N_s + 2c^2(N - N_s)K\lambda^2T}, \quad (26)$$

$$\mathbf{P}_{c\delta t_r}^{f*} = \left[N_s \mathbf{R}_\epsilon^{-1} + \frac{N - N_s}{\sigma_\eta^2} \mathbf{I}_{K \times K} \right]^{-1}, \quad \beta \triangleq \frac{\sigma_{\eta_s}^2}{\sigma_\epsilon^2(1)},$$

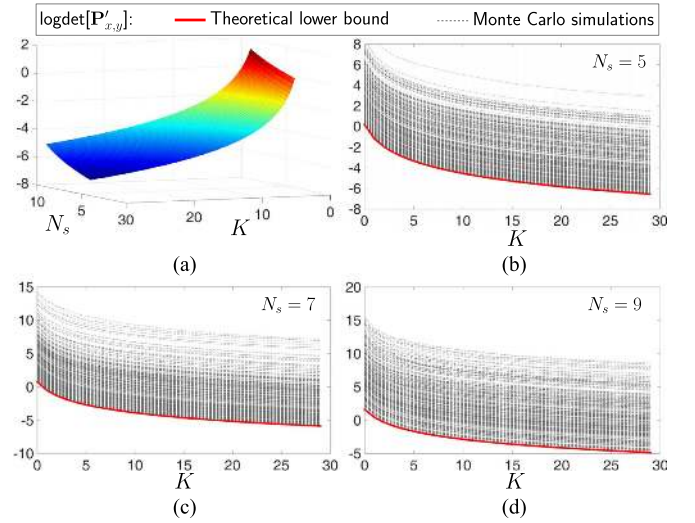


Fig. 5. (a) Surface plot of $\log \det[\mathbf{P}'_{x,y}]$ as a function of N_s and k . (b)–(d) Plots of $\log \det[\mathbf{P}'_{x,y}]$ for 500 Monte Carlo simulations along with the theoretical lower bound $\log \det[\mathbf{P}^{f*}_{x,y}]$. Simulation parameters: $N = 12$, $T = 0.2$ s, $\alpha = 10^{-3}$ Hz, $\sigma_\eta^2 = 4$ m², and $\lambda = 66$ ns/s.

and $f(\beta)$ is a function of β . The expression of $f(\beta)$ and the derivation of (26) are outlined in Appendix C.

Monte Carlo simulations for several N_s and k values were conducted to demonstrate the result in (26). The logarithm of the determinant of each resulting position estimation error covariance $\mathbf{P}'_{x,y}$, namely $\log \det[\mathbf{P}'_{x,y}]$, for 500 runs were plotted along with $\log \det[\mathbf{P}^{f*}_{x,y}]$ obtained in (26). A surface plot of $\log \det[\mathbf{P}'_{x,y}]$ and the Monte Carlo simulation results for $\log \det[\mathbf{P}'_{x,y}]$ are shown in Fig. 5.

The following remarks can be concluded from these simulations.

Remark 1: For a fixed $N_s < N$, $\log \det[\mathbf{P}^{f*}_{x,y}]$ is a strictly decreasing function of K , and it can be concluded that (26) approaches zero as $K \rightarrow \infty$. This implies that a good strategy for the navigator in the presence of sector mismatch is to stand still if it does not have exact knowledge on the change in its position.

Remark 2: For large K , the approximation $f(\beta)N_s\sigma_\eta^2 + 2c^2(N - N_s)K\lambda^2T \approx 2c^2(N - N_s)K\lambda^2T$ can be made, since $f(\beta)N_s\sigma_\eta^2$ is constant for a given σ_η^2 and $\bar{\sigma}_\epsilon^2(1)$, and therefore $2c^2(N - N_s)K\lambda^2T \gg f(\beta)N_s\sigma_\eta^2$ for large K . Subsequently, (26) can be approximated by

$$\mathbf{P}_{x,y}^{f*} \approx \frac{2\sigma_\eta^2\mathbf{I}_{2 \times 2}}{(N - N_s)K}. \quad (27)$$

The same expression is obtained when the navigator uses only the measurements from the $N - N_s$ BTSs with no sector mismatch to estimate its state. This results from the fact that the measurements coming from the N_s BTSs with sector mismatch are highly correlated in time and the uncertainty associated with these measurements is a strictly increasing function of K . Thus, subsequent measurements from BTSs with sector mismatch will bring little to no contribution in estimating the state of the navigator and will therefore be “neglected” by the estimator.

Remark 3: It is also worth noting that when $N_s = N$, the optimal position estimation error covariance becomes

$$\mathbf{P}_{x,y}^{\star} = \frac{4c^2 K \lambda^2 T \mathbf{I}_{2 \times 2}}{f(\beta) \sigma_\eta^2 N},$$

which is a finite constant. In contrast to the point solution case, the need to have at least one measurement coming from a BTS with no mismatch between the mapper and navigator sectors is eliminated in the batch estimator.

D. Practical Upper Bound on the Position Error

This subsection characterizes an upper bound on the position error due to the discrepancy between sectors' clock biases. To this end, it is assumed that $N_s = N$, i.e., the mapping receivers are listening to different sectors than the navigating receiver, and the latter is not aware of the presence of these discrepancies. It is also assumed that the WNLS is in steady state, and the discrepancies $\epsilon = [\epsilon_1, \dots, \epsilon_N]^T$ are suddenly introduced into the measurements, which will induce an incremental change in the receiver state estimate $\delta \mathbf{x}_r = c(\mathbf{H}^T \mathbf{R}_\eta^{-1} \mathbf{H})^{-1} \mathbf{H}^T \mathbf{R}_\eta^{-1} \epsilon$. In general, the discrepancy vector ϵ can be expressed as

$$\epsilon = b \mathbf{1}_N + \psi, \quad (28)$$

where $b \triangleq \frac{1}{N} \sum_{i=1}^N \epsilon_i = \frac{1}{N} \mathbf{1}_N^T \epsilon$, and $\psi \triangleq [\epsilon_1 - b, \dots, \epsilon_N - b]^T$. The term b is referred to as the common error and the vector ψ as the unbiased error. It follows from this definition that $\sum_{i=1}^N \psi_i = 0$. By replacing the expression of ϵ in a WNLS step, the incremental change in the receiver state estimate can be expressed as $\delta \mathbf{x}_r = \delta \mathbf{x}_r^{(b)} + \delta \mathbf{x}_r^{(\psi)}$, where $\delta \mathbf{x}_r^{(b)} = cb(\mathbf{H}^T \mathbf{R}_\eta^{-1} \mathbf{H})^{-1} \mathbf{H}^T \mathbf{R}_\eta^{-1} \mathbf{1}_N$ is the effect of the common error and $\delta \mathbf{x}_r^{(\psi)} = c(\mathbf{H}^T \mathbf{R}_\eta^{-1} \mathbf{H})^{-1} \mathbf{H}^T \mathbf{R}_\eta^{-1} \psi$ is the effect of the unbiased error.

1) *Effect of Common Error on Navigation Solution:* The common error term will only affect the receiver clock bias estimate. This can be shown by realizing that

$$\mathbf{H} \mathbf{e}_3 = [\mathbf{G} \quad \mathbf{1}_N] \mathbf{e}_3 = \mathbf{1}_N, \quad (29)$$

where $\mathbf{e}_3 = [0, 0, 1]^T$. Then, using (29), the incremental change due to the common term becomes

$$\begin{aligned} \delta \mathbf{x}_r^{(b)} &= cb (\mathbf{H}^T \mathbf{R}_\eta^{-1} \mathbf{H})^{-1} \mathbf{H}^T \mathbf{R}_\eta^{-1} \mathbf{1}_N \\ &= cb (\mathbf{H}^T \mathbf{R}_\eta^{-1} \mathbf{H})^{-1} \mathbf{H}^T \mathbf{R}_\eta^{-1} \mathbf{H} \mathbf{e}_3 = cb \mathbf{e}_3, \end{aligned} \quad (30)$$

which has a non-zero component only in the clock bias state. Thus, if the individual discrepancies ϵ_i happen to be all equal, the receiver's position estimate will be unaffected.

2) *Effect of Unbiased Error on Navigation Solution:* Unlike the common error, the unbiased error will affect all receiver states. The following theorem establishes a bound on the error introduced by the unbiased error in the receivers position estimate.

Theorem III.3: In a cellular environment comprising N BTSs in which the mapping and navigating receivers are experiencing bounded sector mismatches ϵ_i , such that $|\epsilon_i| \leq \alpha$, $\forall i$, the error induced by the mismatches in the receiver's

position estimate is bounded by

$$\|\delta \mathbf{r}_r\| \leq \begin{cases} \sqrt{N} \alpha \kappa, & \text{if } N \text{ is even,} \\ \sqrt{\frac{N^2-1}{N}} \alpha \kappa, & \text{if } N \text{ is odd,} \end{cases}$$

where $\kappa \triangleq c \|(\mathbf{H}^T \mathbf{R}_\eta^{-1} \mathbf{H})^{-1} \mathbf{H}^T \mathbf{R}_\eta^{-1}\|$.

Proof: The incremental change in the receiver position state estimate can be expressed as $\delta \mathbf{r}_r = \mathbf{T} \delta \mathbf{x}_r = \mathbf{T} \delta \mathbf{x}_r^{(b)} + \mathbf{T} \delta \mathbf{x}_r^{(\psi)}$, where $\mathbf{T} = [\mathbf{I}_{2 \times 2} \quad \mathbf{0}_{2 \times 1}]$. By replacing $\delta \mathbf{x}_r^{(b)}$ with its expression from (30), the change in position becomes

$$\delta \mathbf{r}_r = cb \mathbf{T} \mathbf{e}_3 + \mathbf{T} \delta \mathbf{x}_r^{(\psi)} = \mathbf{T} \delta \mathbf{x}_r^{(\psi)}. \quad (31)$$

Taking the 2-norm on both sides of (31) yields

$$\begin{aligned} \|\delta \mathbf{r}_r\| &= \|\mathbf{T} \delta \mathbf{x}_r^{(\psi)}\| \\ &\leq \|\mathbf{T}\| \cdot \|\delta \mathbf{x}_r^{(\psi)}\| = \|\delta \mathbf{x}_r^{(\psi)}\|, \end{aligned} \quad (32)$$

since $\|\mathbf{T}\| = 1$. Replacing $\delta \mathbf{x}_r^{(\psi)}$ by its expression in the WNLS update, (32) becomes

$$\begin{aligned} \|\delta \mathbf{r}_r\| &\leq \left\| c (\mathbf{H}^T \mathbf{R}_\eta^{-1} \mathbf{H})^{-1} \mathbf{H}^T \mathbf{R}_\eta^{-1} (\epsilon - b \mathbf{1}_N) \right\| \\ &\leq \kappa \|\epsilon - b \mathbf{1}_N\|. \end{aligned} \quad (33)$$

Therefore, to determine the upper bound of (33), the term $\|\epsilon - b \mathbf{1}_N\|$, or equivalently its square, must be maximized, leading to

$$\begin{aligned} \underset{\epsilon}{\text{maximize}} \quad & \|\epsilon - b \mathbf{1}_N\|^2 = \|\mathbf{A} \epsilon\|^2, \\ \mathbf{A} \triangleq & \begin{bmatrix} (1 - \frac{1}{N}) & -\frac{1}{N} & \cdots & -\frac{1}{N} \\ -\frac{1}{N} & (1 - \frac{1}{N}) & \cdots & -\frac{1}{N} \\ \vdots & \vdots & \ddots & \vdots \\ -\frac{1}{N} & -\frac{1}{N} & \cdots & (1 - \frac{1}{N}) \end{bmatrix}. \end{aligned} \quad (34)$$

Motivated by experimental data collected in different BTS cell sectors and for various cells, it is reasonable to assume that

$$|\epsilon_i| \leq \alpha, \quad \forall i, \quad (35)$$

where α is some positive constant. As such, the maximization problem in (34) becomes constrained by (35). The function in (34) is convex, since it is the composition of the norm with a linear mapping, and the box constraints in (35) form a convex set. Therefore, the maximizer of (34) subject to the constraints (35) lies on the extreme points of the feasibility region, namely $|\epsilon_i^*| = \alpha, \forall i$.

If N is even, the maximum is achieved whenever $\sum_{i=1}^N \epsilon_i = 0$; hence, the maximizer is $\epsilon_i^* = (-1)^i \alpha, \forall i$. If N is odd, the maximum is achieved whenever $\sum_{i=1}^N \epsilon_i = \alpha$; hence, the maximizer is $\epsilon_i^* = (-1)^i \alpha$ for $i = 1, \dots, N-1$, and $\epsilon_N^* = \pm \alpha$. Therefore, the maximum error introduced in the receiver's position is bounded by

$$\|\delta \mathbf{r}_r\| \leq \begin{cases} \sqrt{N} \alpha \kappa, & \text{if } N \text{ is even,} \\ \sqrt{\frac{N^2-1}{N}} \alpha \kappa, & \text{if } N \text{ is odd.} \end{cases}$$

■

IV. EXPERIMENTAL RESULTS

Navigation using the proposed mapper/navigator framework discussed in Section II was tested in three experiments with (1) a mobile ground vehicle and a stationary mapper, (2) a UAV and a stationary mapper, and (3) a UAV and a mobile mapper. In both experiments, the cellular CDMA module of the LabVIEW-based Multichannel Adaptive TRansceiver Information eXtractor (MATRIX) SDR developed in [24] was used to process the cellular CDMA signals, and the Generalized Radionavigation Interfusion Device (GRID) SDR [49] was used to process the GPS signals. The measurement noise variance for the mapper and navigator was calculated from [41]

$$\sigma_i^2 = \frac{c^2 B_{n,DLL} q(t_{eml})}{2(C/N_0)_i (1 - 2B_{n,DLL} T_{CO})}, \quad (36)$$

where t_{eml} is the early-minus-late time in the CDMA receiver's delay-locked loop (DLL) correlators (expressed in chips), $B_{n,DLL}$ is the DLL loop noise bandwidth (expressed in Hertz), $(C/N_0)_i$ is the measured carrier-to-noise ratio for the i th BTS (expressed in Hertz), $T_{CO} = \frac{1}{37.5}$ s is the predetection coherent integration time, and $q(t_{eml})$ is a function of the autocorrelation of the cellular CDMA short code, whose expression is given in [41]. Moreover, the three-dimensional (3-D) position states of the BTSs involved in the experiments were mapped prior to the experiments according to the framework discussed in [32]. The following subsections present results for each experiment.

A. Ground Vehicle Results

In this experiment, two cars (a mapper and a navigator) were equipped with two antennas each to acquire and track: (1) GPS signals and (2) signals from nearby cellular CDMA BTSs. The receivers' CDMA antennas used for the experiment were consumer-grade 800/1900 MHz cellular antennas, and the GPS antennas were surveyor-grade Leica antennas. The GPS and cellular signals were simultaneously down-mixed and synchronously sampled via two universal software radio peripherals (USRPs) driven by the same GPS-disciplined oscillator (GSPDO). The receivers were tuned to the cellular carrier frequency 882.75 MHz, which is a channel allocated for U.S. cellular provider Verizon Wireless. Samples of the received signals were stored for off-line post-processing. Over the course of the experiment, both receivers were listening to the same 3 BTSs. The mapping receiver and the navigating receiver were listening to the same sectors; hence, there were no additional errors due to the discrepancies between sector clocks. The mapping receiver was stationary during the experiments and was estimating the clock biases of the 3 BTSs with known position states via a WLS estimator as discussed in Subsection II-B. The BTSs' position states were expressed in a local 3-D frame whose horizontal plane passes through the three BTSs and is centered at the mean of the BTSs' positions. The height of the navigator was known and constant in the local 3-D frame over the trajectory driven and was passed as a constant parameter to the estimator. Hence, only the navigator's two-dimensional (2-D) position and its clock bias were estimated through the WNLS described in Subsection II-E. The weights of the WNLS were calculated



Fig. 6. Experimental hardware setup, navigator trajectory, and mapper and BTS locations for ground experiments. Map data: Google Earth.

using (36). For the first pseudorange measurement, the WNLS iterations were initialized by setting the navigator's initial horizontal position states at the origin of the 3-D local frame and the initial clock bias to zero. For each subsequent pseudorange measurement, the WNLS iterations were initialized at the solution from the previous WNLS. The experimental hardware setup, the environment layout, and the true and estimated navigator trajectories are shown in Fig. 6.

It can be seen from Fig. 6 that the navigation solution obtained from the cellular CDMA signals follows closely the navigation solution obtained using GPS signals. The mean distance difference along the traversed trajectory between the GPS and CDMA navigation solutions was calculated to be 5.51 m with a standard deviation of 4.01 m and a maximum error of 11.11 m. The mean receiver clock estimate difference between the GPS and CDMA navigation solutions was calculated to be -45 ns with a standard deviation of 23.03 ns.

B. UAV Results

Two UAV experiments were conducted: (1) one with a stationary mapper and (2) one with a mobile mapper.

1) *UAV Results With a Stationary Mapper:* In this experiment, the mapper consisted of a GSPDO-driven dual-channel USRP connected to a high-gain tri-band cellular antenna and a surveyor-grade Leica GPS antenna deployed on the roof of Winston Chung Hall at the University of California, Riverside. A DJI Matrice 600 UAV was used as the navigator, which was

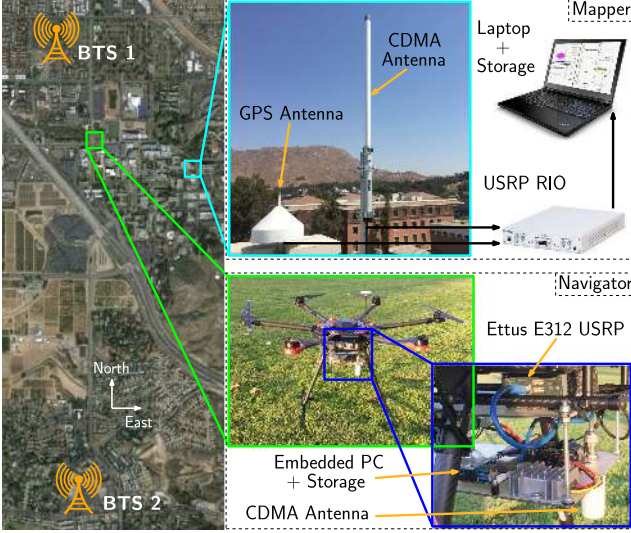


Fig. 7. SOP BTS environment and experimental hardware setup with stationary mapper. Map data: Google Earth.

equipped with a consumer-grade 800/1900 MHz cellular antenna and a small consumer-grade GPS antenna to discipline the on-board oscillator. The cellular signals on the navigator side were down-mixed and sampled by a single-channel Ettus E312 USRP driven by a GPS-disciplined temperature compensated crystal oscillator (TCXO). The cellular receivers were tuned to the cellular carrier frequency 883.98 MHz, which is also a channel allocated for Verizon Wireless. Samples of the received signals were stored for off-line post-processing. The ground-truth reference for the navigator trajectory was taken from the UAV's on-board navigation system, which uses GPS, inertial navigation system, and other sensors. Fig. 7 shows the SOP BTS environment in which the mapper and navigator were present as well as the experimental hardware setup, which is similar to the one employed in [40], [41].

Over the course of the experiment, the mapper and the navigator were listening to the same 2 BTSs. Since only 2 BTSs were available for processing, an extended Kalman filter (EKF) framework was adopted (for observability considerations) to estimate the navigator's state \mathbf{x}_r , which is composed of its 2-D position \mathbf{r}_r , velocity $\dot{\mathbf{r}}_r$, clock bias δt_r , and clock drift $\dot{\delta t}_r$, namely $\mathbf{x}_r \triangleq [\mathbf{r}_r^T, \dot{\mathbf{r}}_r^T, \delta t_r, \dot{\delta t}_r]^T$. Similarly to the ground experiment, all position states were expressed in a local 3-D frame whose horizontal plane is defined by the two BTSs and the mapper and is centered at the mean of two BTSs' and the mapper's positions. The UAV was programmed to fly at a constant height and at a constant speed. Hence, similarly to the ground experiment, the height of the navigator was passed as a constant parameter to the filter. The navigator's position and velocity states were assumed to evolve according to velocity random walk dynamics, and the clock bias and clock drift dynamics were modeled according to the standard clock error model: double integrator driven by noise, as discussed in [9]. The power spectral densities of the process noise driving \ddot{x}_r and \ddot{y}_r were obtained by post-processing the data sampled from the UAV's on-board navigation system. The time averages of the x and y accelerations were approximately zero with time variances $\sigma_{\ddot{x}}^2 \approx 0.36 \text{ (m/s}^2\text{)}^2$

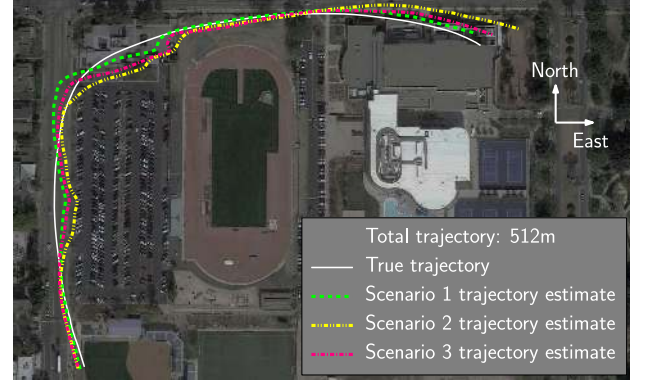


Fig. 8. UAV's true and estimated trajectories for a stationary mapper. Map data: Google Earth.

and $\sigma_{\ddot{y}}^2 \approx 0.24 \text{ (m/s}^2\text{)}^2$. These variances were used to form the covariance matrix of the process noise driving the position and velocity states [9]. Alternatively, the power spectra of the acceleration process noise may be estimated adaptively [31], or an inertial measurement unit (IMU) may be used to propagate the position and orientation states of the navigator. The process noise covariance of the clock error states can be parameterized by the white frequency coefficient h_0 and the frequency random walk coefficient h_{-2} [50], [51]. Since the USRP on-board the navigator is equipped with a TCXO, the aforementioned coefficients were chosen to be $h_0 = 9.4 \times 10^{-20}$ and $h_{-2} = 3.8 \times 10^{-21}$ [31]. The EKF states corresponding to the UAV's position and velocity were initialized with the values obtained from the on-board navigation system with a zero initial uncertainty. The EKF state corresponding to the clock bias was initialized according to

$$c\hat{\delta t}_r(0| - 1) = \rho_1(0) - \|\mathbf{r}_r(0) - \mathbf{r}_{s_1}\|_2 + c\hat{\delta t}_{s_1}(0),$$

where $\mathbf{r}_r(0)$ is the UAV's initial position obtained from the on-board navigation system and $\hat{\delta t}_{s_1}(0)$ is the first BTS's clock bias estimate given by the mapper at $k = 0$. The initial uncertainty associated with $c\hat{\delta t}_r(0| - 1)$ was set equal to the estimation error variance $\sigma_{\delta t_{s_1}}^2$ given by the mapper. The EKF state corresponding to the clock drift was initialized to zero with an initial uncertainty of $10 \text{ (m/s}^2\text{)}^2$. The measurement noise covariance matrix was obtained using (20) and (36). Three scenarios were tested. In the first scenario, the mapper and the navigator were listening to the same sectors; hence, there were no additional errors due to the discrepancies between sector clocks. In the second scenario, the mapper was forced to listen to a different sector of BTS 1 than the navigator; however, the measurement noise covariance was not modified to compensate for the discrepancy introduced. The third scenario is similar to the second, except that the measurement noise covariance was modified to account for the sector clock bias discrepancy, as defined in (20). The initial discrepancy was calculated and was known to the EKF for scenarios 2 and 3. Moreover, the parameters λ and α were calculated offline by the mapper and were found to be $\lambda = 13 \text{ ns/s}$ and $\alpha = 8 \times 10^{-4} \text{ Hz}$. The navigator's true trajectory and estimated trajectory for each scenario are shown in Fig. 8 and the resulting RMSEs are tabulated in Table I.

TABLE I
EXPERIMENTAL RESULTS FOR UAV WITH STATIONARY MAPPER

	Scenario 1	Scenario 2	Scenario 3
RMSE (m)	9.39	23.99	13.42
Standard deviation (m)	3.42	11.24	5.18
Maximum error (m)	18.96	38.93	31.98

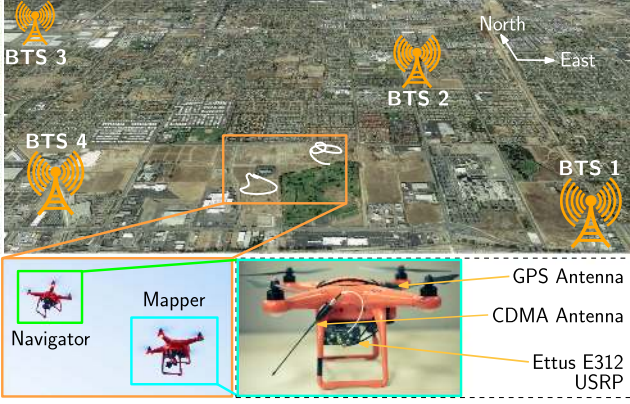


Fig. 9. SOP BTS environment and experimental hardware setup with a mobile mapper. Map data: Google Earth.

Fig. 8 and Table I show a significant improvement in the estimation performance when the sector clock bias error model identified in this paper is used, which is reflected in a reduction of around 11 m in the RMSE, 6 m in the standard deviation, and 7 m in the maximum error. Note that the UAV position estimate deviates from the true trajectory initially even though the UAV had not performed sharp maneuvers. This is due to the error in the pseudorange measurements caused by multipath. These multipath errors are not negligible, since the UAV is flying slightly lower than the BTSs, which are located around 1 and 2.3 km away from the UAVs.

2) *UAV Results With a Mobile Mapper*: In this experiment, the mapper and the navigator were identical Autel Robotics X-Star Premium UAVs equipped with a single-channel Ettus E312 USRP driven by a GPS-disciplined TCXO connected to a consumer-grade 800/1900 MHz cellular antenna and a small consumer-grade GPS antenna to discipline the on-board oscillator. The cellular receivers were tuned to the cellular carrier frequency 882.75 MHz, which is also a channel allocated for Verizon Wireless. Samples of the received signals were stored for off-line post-processing. The ground-truth references for the mapper and navigator trajectories were taken from the UAVs' on-board navigation systems, which use GPS, inertial navigation system, and other sensors. Note that in this scenario, the clock biases were taken with respect to the mapper's clock bias. Fig. 9 shows the SOP BTS environment in which the mapper and navigator were present as well as the experimental hardware setup.

Over the course of the experiment, the mapper and the navigator were listening to the same 4 BTSs. The same three scenarios performed in the stationary mapper experiment were considered. In this case, SOP BTS 4 was the BTS cell in which the mapper and the navigator were listening to different sectors. The framework discussed in Subsection II-E was adopted. The

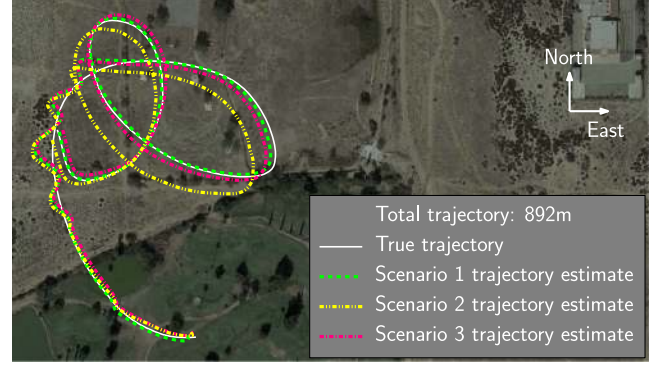


Fig. 10. UAV's true and estimated trajectories for a mobile mapper. Map data: Google Earth.

TABLE II
EXPERIMENTAL RESULTS FOR UAV WITH A MOBILE MAPPER

	Scenario 1	Scenario 2	Scenario 3
RMSE (m)	5.05	13.70	6.66
Standard deviation (m)	3.12	7.00	3.27
Maximum error (m)	16.67	23.77	16.86

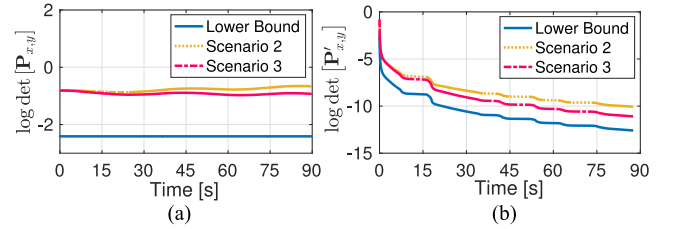


Fig. 11. Logarithm of the determinant of the position estimation error covariance for (a) the point solution and (b) the batch estimator for scenarios 2 and 3. The theoretical lower bounds are also plotted.

initial discrepancy was calculated and was known to the WNLS for scenarios 2 and 3. Moreover, the parameters λ and α were calculated offline by the mapper and were found to be $\lambda = 15.28$ ns/s and $\alpha = 2.2 \times 10^{-4}$ Hz. The navigator's true trajectory and estimated trajectory for each scenario are shown in Fig. 10 and the resulting RMSEs are tabulated in Table II.

Fig. 10 and Table II show a significant improvement in the estimation performance when the sector clock bias error model identified in this paper is used, which is reflected in a reduction of around 7 m in the RMSE, a reduction of 3.7 m in the standard deviation, and a reduction of 7 m in the maximum error. It is worth mentioning that the position RMSE obtained by not using SOP BTS 4 was around 11 m. This indicates that not using the BTS in case of sector mismatch is not the best strategy. A better performance may be obtained by exploiting all available BTSs' and incorporating the rigorous error models derived in this paper.

Fig. 11 shows $\log \det[\mathbf{P}_{x,y}]$ and $\log \det[\mathbf{P}'_{x,y}]$ for a point solution and a batch estimator, respectively, corresponding to the experimental results of scenarios 2 and 3 along with the theoretical lower bounds derived in Subsections III-B and III-C. It can be seen that scenario 3 outperforms scenario 2 in terms of estimation error uncertainty for both estimators. Moreover, the lower bounds are never violated. The difference between

the experimental logarithm of the determinant of the position estimation error covariance and the theoretical lower bound is attributed to the geometrical configuration of the BTSs, which does not meet the optimal requirements in Theorem III.2.

Remark Comparing the proposed navigation approach with the state-of-the-art in the literature is not straightforward, since cellular CDMA navigation receivers were not documented in a way that facilitates reproduction (they are mainly proprietary, e.g., [22]). Part I of this paper extensively discusses a receiver architecture for navigation with cellular CDMA signals. Moreover, the navigation frameworks proposed in the literature are significantly different than the mapper/navigator framework proposed in this work. In addition, to the authors' knowledge, this paper is the first to demonstrate UAVs navigating with cellular CDMA signals. While a 1.68 m error has been reported by combining cellular CDMA and digital television signals in the literature [22], this paper reports 5 m accuracy using cellular CDMA signals exclusively.

V. CONCLUSION

This paper studied a navigation framework consisting of a mapping and a navigating receiver in a cellular CDMA environment. Theoretical lower bounds on the navigation performance under errors due to the discrepancy between BTS sector clock biases were derived and analyzed. Moreover, a lower bound on the logarithm of the determinant of the estimation error covariance was derived for non-identical measurement noise variances and a receiver-BTS configuration that achieves this bound was identified. A practical upper bound on the position error due to the discrepancy between sector clock biases was characterized. Also, two sets of experimental results were presented: one for a ground vehicle and one for a UAV. The first experiment compared the navigation solution from GPS versus that of cellular CDMA and showed a mean distance difference of 5.51 m in the absence of sector clock bias discrepancies. The second experiment showed an improvement of nearly 11 m in the RMSE when the discrepancy is accounted for utilizing the statistical model relating observed clock biases from different sectors of the same BTS cell.

APPENDIX A

DERIVATION OF EQUATION (23)

Using (21), the limit of $\log \det[\mathbf{P}_{x,y}^*]$ can be expressed as

$$\begin{aligned} \lim_{k \rightarrow \infty} \log \det [\mathbf{P}_{x,y}^*] &= \lim_{k \rightarrow \infty} \log \left[4 (\sigma_{\text{eq}}^2)^2 \right] \\ &= \log \left[4 \left(\lim_{k \rightarrow \infty} \sigma_{\text{eq}}^2 \right)^2 \right], \end{aligned} \quad (37)$$

It follows from (22) that

$$\begin{aligned} \lim_{k \rightarrow \infty} \sigma_{\text{eq}}^2 &= \frac{\left(\sigma_{\eta}^2 + \frac{c^2 \lambda^2}{\alpha} \right) \sigma_{\eta}^2}{N \sigma_{\eta}^2 + (N - N_s) \frac{c^2 \lambda^2}{\alpha}} \\ &= \frac{\left(1 + \frac{\sigma_{\eta}^2}{\frac{c^2 \lambda^2}{\alpha}} \right) \sigma_{\eta}^2}{N \frac{\sigma_{\eta}^2}{\frac{c^2 \lambda^2}{\alpha}} + (N - N_s)}. \end{aligned} \quad (38)$$

Based on experimental data [41], $\sigma_{\eta} \approx 1$ to 2 m, $c\lambda \approx 0.4$ to 4 m, and $\alpha \approx 10^{-4}$ to 10^{-3} Hz. Therefore, the ratio $\frac{\sigma_{\eta}^2}{\frac{c^2 \lambda^2}{\alpha}}$ is negligible, hence

$$\lim_{k \rightarrow \infty} \sigma_{\text{eq}}^2 \approx \frac{\sigma_{\eta}^2}{N - N_s},$$

therefore (37) becomes

$$\lim_{k \rightarrow \infty} \log \det [\mathbf{P}_{x,y}^*] \approx \log \left[4 \left(\frac{\sigma_{\eta}^2}{N - N_s} \right)^2 \right].$$

APPENDIX B

DERIVATION OF EQUATION (24)

Using (21), $\log \det[\mathbf{P}_{x,y}^*]$ can be expressed as

$$\begin{aligned} \log \det [\mathbf{P}_{x,y}^*] &= \log \left[4 (\sigma_{\text{eq}}^2)^2 \right] \\ &= \log(4) - 2 \log \left(\frac{1}{\sigma_{\text{eq}}^2} \right), \end{aligned} \quad (39)$$

Noting that $\sigma_{\text{eq}}^2 = \frac{\sigma_{\eta}^2 [\sigma_{\eta}^2 + \sigma_{\epsilon}^2(k)]}{N_s \sigma_{\eta}^2 + (N - N_s) [\sigma_{\eta}^2 + \sigma_{\epsilon}^2(k)]}$, (39) becomes

$$\begin{aligned} \log \det [\mathbf{P}_{x,y}^*] &= \log(4) - 2 \log \left[\frac{N_s}{\sigma_{\eta}^2 + \sigma_{\epsilon}^2(k)} + \frac{N}{\sigma_{\eta}^2} - \frac{N_s}{\sigma_{\eta}^2} \right] \\ &= \log(4) - 2 \log \left\{ \frac{N}{\sigma_{\eta}^2} \left[1 - \frac{N_s}{N} \left(1 - \frac{\sigma_{\eta}^2}{\sigma_{\eta}^2 + \sigma_{\epsilon}^2(k)} \right) \right] \right\} \\ &= -2 \log \left[1 - \frac{N_s}{N} \left(1 - \frac{\sigma_{\eta}^2}{\sigma_{\eta}^2 + \sigma_{\epsilon}^2(k)} \right) \right] \\ &\quad + \underbrace{\log(4) - 2 \log \left(\frac{N}{\sigma_{\eta}^2} \right)}_{\triangleq \xi \text{ (constant)}}. \end{aligned}$$

For large k , the ratio $\frac{\sigma_{\eta}^2}{\sigma_{\eta}^2 + \sigma_{\epsilon}^2(k)} = 1 - \frac{1}{1 + \frac{\sigma_{\eta}^2}{\sigma_{\epsilon}^2(k)}}$ becomes negligible (see Appendix A), therefore

$$\log \det [\mathbf{P}_{x,y}^*] \approx -2 \log \left(1 - \frac{N_s}{N} \right) + \xi.$$

APPENDIX C

DERIVATION OF EQUATION (26)

In this appendix, the expression for the optimal estimation error covariance for the batch estimator given in (26) is derived. From (25), $\bar{\sigma}_{\epsilon}^2(k)$ may be expressed as $\bar{\sigma}_{\epsilon}^2(k) = k \bar{\sigma}_{\epsilon}^2(1)$. Therefore, the elements of \mathbf{R}_{ϵ} can be approximated by $[\mathbf{R}_{\epsilon}]_{m,n} \approx \min\{m, n\} \bar{\sigma}_{\epsilon}^2(1)$, hence

$$\mathbf{R}_{\epsilon} \approx \bar{\sigma}_{\epsilon}^2(1) \mathbf{\Gamma}_K,$$

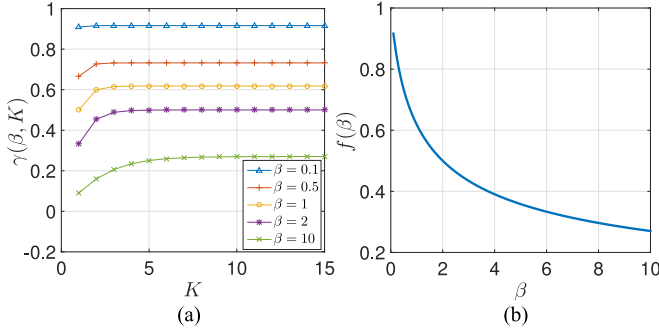


Fig. 12. Plot of (a) $\gamma(\beta, K)$ and (b) $f(\beta) = \gamma(\beta, K_0)$ where $K_0 > 10$.

where $[\Gamma_K]_{m,n} = \min\{m, n\}$, $m, n = 1, \dots, K$. For the batch estimator, the sum $\sum_{l=1}^L N_l \mathbf{1}_K^T \mathbf{R}_l^{-1} \mathbf{1}_K$ becomes

$$\begin{aligned} \sum_{l=1}^L N_l \mathbf{1}_K^T \mathbf{R}_l^{-1} \mathbf{1}_K &= N_s \mathbf{1}_K^T (\sigma_\eta^2 \mathbf{I}_{K \times K} + \mathbf{R}_\epsilon)^{-1} \mathbf{1}_K \\ &\quad + (N - N_s) \mathbf{1}_K^T (\sigma_\eta^2 \mathbf{I}_{K \times K})^{-1} \mathbf{1}_K \\ &= N_s \mathbf{1}_K^T (\sigma_\eta^2 \mathbf{I}_{K \times K} + \bar{\sigma}_\epsilon^2(1) \Gamma_K)^{-1} \mathbf{1}_K \\ &\quad + \frac{(N - N_s) K}{\sigma_\eta^2} \\ &= \frac{N_s}{\bar{\sigma}_\epsilon^2(1)} \mathbf{1}_K^T \left(\frac{\sigma_\eta^2}{\bar{\sigma}_\epsilon^2(1)} \mathbf{I}_{K \times K} + \Gamma_K \right)^{-1} \mathbf{1}_K \\ &\quad + \frac{(N - N_s) K}{\sigma_\eta^2}. \end{aligned}$$

By defining $\beta \triangleq \frac{\sigma_\eta^2}{\bar{\sigma}_\epsilon^2(1)}$ and $\gamma(\beta, K) \triangleq \mathbf{1}_K^T (\beta \mathbf{I}_{K \times K} + \Gamma_K)^{-1} \mathbf{1}_K$, the above expression simplifies to

$$\sum_{l=1}^L N_l \mathbf{1}_K^T \mathbf{R}_l^{-1} \mathbf{1}_K = \frac{N_s}{\bar{\sigma}_\epsilon^2(1)} \gamma(\beta, K) + \frac{(N - N_s) K}{\sigma_\eta^2}. \quad (40)$$

It can be shown that $\Gamma_K = \mathbf{U} \mathbf{U}^T$, where \mathbf{U} is a lower triangular matrix with all its nonzero elements equal to one. Subsequently, using the matrix inversion lemma, $\gamma(\beta, K)$ can be expressed as

$$\gamma(\beta, K) = \mathbf{1}_K^T \left[\frac{1}{\beta} \mathbf{I} - \frac{1}{\beta^2} \mathbf{U} \left(\mathbf{I} + \frac{1}{\beta} \mathbf{U}^T \mathbf{U} \right)^{-1} \mathbf{U}^T \right] \mathbf{1}_K,$$

where the $K \times K$ subscript on the identity matrices is dropped for compactness of notation. The above expression may be expressed as

$$\gamma(\beta, K) = \frac{K}{\beta} \left[1 - \frac{1}{K\beta} \mathbf{1}_K^T \mathbf{U} (\beta \mathbf{I} + \mathbf{U}^T \mathbf{U})^{-1} \mathbf{U}^T \mathbf{1}_K \right].$$

A plot of $\gamma(\beta, K)$ as a function of K and β is shown in Fig. 12 (a). It can be seen that for a given β , $\gamma(\beta, K)$ approaches a finite value for relatively large K . This function is defined as $f(\beta) = \gamma(\beta, K_0)$, where $K_0 > 10$, and is shown in Fig. 12 (b). Note that $f(\beta)$ in Fig. 12 (b) was obtained by evaluating $\gamma(\beta, K)$ at $K = 15$.

For large K (greater than 10), (40) becomes

$$\sum_{l=1}^L N_l \mathbf{1}_K^T \mathbf{R}_l^{-1} \mathbf{1}_K = \frac{N_s f(\beta) \sigma_\eta^2 + (N - N_s) K \bar{\sigma}_\epsilon^2(1)}{\bar{\sigma}_\epsilon^2(1) \sigma_\eta^2}. \quad (41)$$

It follows from the definition of \mathbf{R} that

$$\sum_{l=1}^L N_l \mathbf{R}_l^{-1} = N_s \mathbf{R}_\epsilon^{-1} + \frac{(N - N_s)}{\sigma_\eta^2} \mathbf{I}_{K \times K}. \quad (42)$$

From (41)–(42) and (18) in Theorem III.2, the estimation error covariance matrix with the minimum determinant is given by (26).

ACKNOWLEDGMENT

The authors would like to thank Joshua Morales, Kimia Shamaei, Souradeep Bhattacharya, Yuanqi Gao, and Keshav Narayan for their help in data collection.

REFERENCES

- [1] S. Ji, W. Chen, X. Ding, Y. Chen, C. Zhao, and C. Hu, "Potential benefits of GPS/GLONASS/GALILEO integration in an Urban Canyon—Hong Kong," *J. Navig.*, vol. 63, pp. 681–693, Oct. 2010.
- [2] J. Grabowski, "Personal privacy jammers: Locating Jersey PPDs jamming GBAS safety-of-life signals," *GPS World Mag.*, vol. 23, pp. 28–37, Apr. 2012.
- [3] M. Psiaki and T. Humphreys, "GNSS spoofing and detection," *Proc. IEEE*, vol. 104, no. 6, pp. 1258–1270, Jun. 2016.
- [4] J. Raquet and R. Martin, "Non-GNSS radio frequency navigation," in *Proc. IEEE Acoust., Speech, Signal Process.*, Mar. 2008, pp. 5308–5311.
- [5] L. Merry, R. Faragher, and S. Schedin, "Comparison of opportunistic signals for localisation," in *Proc. IFAC Symp. Intell. Auton. Veh.*, Sep. 2010, pp. 109–114.
- [6] Z. Kassas, "Collaborative opportunistic navigation," *IEEE Aerosp. Electron. Syst. Mag.*, vol. 28, no. 6, pp. 38–41, Jun. 2013.
- [7] Z. Kassas, "Analysis and synthesis of collaborative opportunistic navigation systems," Ph.D. dissertation, Univ. Texas Austin, Austin, TX, USA, 2014.
- [8] Z. Kassas and T. Humphreys, "Observability and estimability of collaborative opportunistic navigation with pseudorange measurements," in *Proc. Inst. Navig. GNSS Conf.*, Sep. 2012, pp. 621–630.
- [9] Z. Kassas and T. Humphreys, "Observability analysis of collaborative opportunistic navigation with pseudorange measurements," *IEEE Trans. Intell. Transp. Syst.*, vol. 15, no. 1, pp. 260–273, Feb. 2014.
- [10] Z. Kassas and T. Humphreys, "Motion planning for optimal information gathering in opportunistic navigation systems," in *Proc. AIAA Guid., Navig., Control Conf.*, Aug. 2013, Paper 551–4565.
- [11] Z. Kassas, A. Arapostathis, and T. Humphreys, "Greedy motion planning for simultaneous signal landscape mapping and receiver localization," *IEEE J. Sel. Topics Signal Process.*, vol. 9, no. 2, pp. 247–258, Mar. 2015.
- [12] Z. Kassas and T. Humphreys, "Receding horizon trajectory optimization in opportunistic navigation environments," *IEEE Trans. Aerosp. Electron. Syst.*, vol. 51, no. 2, pp. 866–877, Apr. 2015.
- [13] Z. Kassas and T. Humphreys, "The price of anarchy in active signal landscape map building," in *Proc. IEEE Global Conf. Signal Inf. Process.*, Dec. 2013, pp. 165–168.
- [14] J. McEllroy, "Navigation using signals of opportunity in the AM transmission band," Master's thesis, Air Force Inst. Technol., Wright-Patterson Air Force Base, OH, USA, 2006.
- [15] S. Fang, J. Chen, H. Huang, and T. Lin, "Is FM a RF-based positioning solution in a metropolitan-scale environment? A probabilistic approach with radio measurements analysis," *IEEE Trans. Broadcast.*, vol. 55, no. 3, pp. 577–588, Sep. 2009.
- [16] M. Joerger, L. Gratton, B. Pervan, and C. Cohen, "Analysis of Iridium-augmented GPS for floating carrier phase positioning," *J. Inst. Navig.*, vol. 57, pp. 137–160, 2010.

- [17] K. Pesyna, Z. Kassas, and T. Humphreys, "Constructing a continuous phase time history from TDMA signals for opportunistic navigation," in *Proc. IEEE/ION Position, Location, Navig. Symp.*, Apr. 2012, pp. 1209–1220.
- [18] M. Rabinowitz and J. Spilker, Jr., "A new positioning system using television synchronization signals," *IEEE Trans. Broadcast.*, vol. 51, no. 1, pp. 51–61, Mar. 2005.
- [19] P. Thevenon *et al.*, "Positioning using mobile TV based on the DVB-SH standard," *J. Inst. Navig.*, vol. 58, pp. 71–90, 2011.
- [20] F. Caron, M. Davy, E. Duflos, and P. Vanheeghe, "Particle filtering for multisensor data fusion with switching observation models: Application to land vehicle positioning," *IEEE Trans. Signal Process.*, vol. 55, no. 6, pp. 2703–2719, Jun. 2007.
- [21] M. Ibrahim and M. Youssef, "CellSense: An accurate energy-efficient GSM positioning system," *IEEE Trans. Veh. Technol.*, vol. 61, no. 1, pp. 286–296, Jan. 2012.
- [22] C. Yang, T. Nguyen, and E. Blasch, "Mobile positioning via fusion of mixed signals of opportunity," *IEEE Aerosp. Electron. Syst. Mag.*, vol. 29, no. 4, pp. 34–46, Apr. 2014.
- [23] Y. Wu, J. Wang, and D. Hu, "A new technique for INS/GNSS attitude and parameter estimation using online optimization," *IEEE Trans. Signal Process.*, vol. 62, no. 10, pp. 2642–2655, May 2014.
- [24] J. Khalife, K. Shamaei, and Z. Kassas, "A software-defined receiver architecture for cellular CDMA-based navigation," in *Proc. IEEE/ION Position, Location, Navig. Symp.*, Apr. 2016, pp. 816–826.
- [25] K. Shamaei, J. Khalife, and Z. Kassas, "Performance characterization of positioning in LTE systems," in *Proc. Inst. Navig. GNSS Conf.*, Sep. 2016, pp. 2262–2270.
- [26] R. Faragher, C. Sarno, and M. Newman, "Opportunistic radio SLAM for indoor navigation using smartphone sensors," in *Proc. IEEE/ION Position, Location, Navig. Symp.*, Apr. 2012, pp. 120–128.
- [27] J. Khalife, Z. Kassas, and S. Saab, "Indoor localization based on floor plans and power maps: Non-line of sight to virtual line of sight," in *Proc. Inst. Navig. GNSS Conf.*, Sep. 2015, pp. 2291–2300.
- [28] J. Prieto, S. Mazuelas, A. Bahillo, P. Fernandez, R. Lorenzo, and E. Abril, "Adaptive data fusion for wireless localization in harsh environments," *IEEE Trans. Signal Process.*, vol. 60, no. 4, pp. 1585–1596, Apr. 2012.
- [29] *Mobile Station-Base Station Compatibility Standard for Dual-Mode Spread Spectrum Systems*, TIA/EIA-95-B, Oct. 1998.
- [30] B. Horn, "How to install a cellular repeater," 2014. [Online]. Available: <http://people.csail.mit.edu/bkph/CellTracker>
- [31] Z. Kassas, V. Ghadiok, and T. Humphreys, "Adaptive estimation of signals of opportunity," in *Proc. Inst. Navig. GNSS Conf.*, Sep. 2014, pp. 1679–1689.
- [32] J. Morales and Z. Kassas, "Optimal collaborative mapping of terrestrial transmitters: Receiver placement and performance characterization," *IEEE Trans. Aerosp. Electron. Syst.*, to be published.
- [33] M. Bshara, U. Orguner, F. Gustafsson, and L. Van Biesen, "Robust tracking in cellular networks using HMM filters and cell-ID measurements," *IEEE Trans. Veh. Technol.*, vol. 60, no. 3, pp. 1016–1024, Mar. 2011.
- [34] R. Martin, C. Yan, H. Fan, and C. Rondeau, "Algorithms and bounds for distributed TDOA-based positioning using OFDM signals," *IEEE Trans. Signal Process.*, vol. 59, no. 3, pp. 1255–1268, Mar. 2011.
- [35] Z. Abu-Shaban, X. Zhou, and T. Abhayapala, "A novel TOA-based mobile localization technique under mixed LOS/NLOS conditions for cellular networks," *IEEE Trans. Veh. Technol.*, vol. 65, no. 11, pp. 8841–8853, Nov. 2016.
- [36] J. Morales, P. Roysdon, and Z. Kassas, "Signals of opportunity aided inertial navigation," in *Proc. Inst. Navig. GNSS Conf.*, Sep. 2016, pp. 1492–1501.
- [37] M. Tsatsanis and Z. Xu, "Performance analysis of minimum variance CDMA receivers," *IEEE Trans. Signal Process.*, vol. 46, no. 11, pp. 3014–3022, Nov. 1998.
- [38] Z. Xu, "Effects of imperfect blind channel estimation on performance of linear CDMA receivers," *IEEE Trans. Signal Process.*, vol. 52, no. 10, pp. 2873–2884, Oct. 2004.
- [39] K. Zarifi and A. Gershman, "High SNR performance analysis of blind minimum output energy receivers for large DS-CDMA systems," *IEEE Trans. Signal Process.*, vol. 56, no. 7, pp. 3248–3260, Jul. 2008.
- [40] J. Khalife and Z. Kassas, "Modeling and analysis of sector clock bias mismatch for navigation with cellular signals," in *Proc. Amer. Control Conf.*, May 2017, pp. 3573–3578.
- [41] J. Khalife, K. Shamaei, and Z. Kassas, "Navigation with cellular CDMA signals—Part I: Signal modeling and software-defined receiver design," *IEEE Trans. Signal Process.*, vol. 66, no. 8, pp. 2191–2203, 2018.
- [42] I. Sharp, K. Yu, and Y. Guo, "GDOP analysis for positioning system design," *IEEE Trans. Veh. Technol.*, vol. 58, no. 7, pp. 3371–3382, Sep. 2009.
- [43] J. Perez-Ramirez, D. Borah, and D. Voelz, "Optimal 3-D landmark placement for vehicle localization using heterogeneous sensors," *IEEE Trans. Veh. Technol.*, vol. 62, no. 7, pp. 2987–2999, Sep. 2013.
- [44] P. Misra and P. Enge, *Global Positioning System: Signals, Measurements, and Performance*, 2nd ed. Lincoln, MA, USA: Ganga-Jamuna Press, 2010.
- [45] J. Khalife and Z. Kassas, "Characterization of sector clock biases in cellular CDMA systems," in *Proc. Inst. Navig. GNSS Conf.*, Sep. 2016, pp. 2281–2285.
- [46] D. Uciński, *Optimal Measurement Methods for Distributed Parameter System Identification*. Boca Raton, FL, USA: CRC Press, 2005.
- [47] P. Massatt and K. Rudnick, "Geometric formulas for dilution of precision calculations," *J. Inst. Navig.*, vol. 37, pp. 379–391, Dec. 1990.
- [48] N. Levanon, "Lowest GDOP in 2-D scenarios," *Inst. Elect. Eng. Proc.—Radar, Sonar Navig.*, vol. 147, pp. 149–155, Jun. 2000.
- [49] T. Humphreys, J. Bhatti, T. Pany, B. Ledvina, and B. O'Hanlon, "Exploiting multicore technology in software-defined GNSS receivers," in *Proc. Inst. Navig. GNSS Conf.*, Sep. 2009, pp. 326–338.
- [50] A. Thompson, J. Moran, and G. Swenson, *Interferometry and Synthesis in Radio Astronomy*, 2nd ed. Hoboken, NJ, USA: Wiley, 2001.
- [51] Y. Bar-Shalom, X. Li, and T. Kirubarajan, *Estimation With Applications to Tracking and Navigation*. New York, NY, USA: Wiley, 2002.



transportation systems.

Joe Khalife (S'15) received the B.S. (with Distinction) degree in electrical engineering and the M.S. degree in computer engineering from the Lebanese American University, Byblos, Lebanon. He is currently working toward the Ph.D. degree in electrical and computer engineering at The University of California, Riverside, Riverside, CA, USA. He is a member of the Autonomous Systems Perception, Intelligence, and Navigation Laboratory. His research interests include estimation, navigation, software-defined receiver design, autonomous vehicles, and intelligent



and Dynamical Systems Simulation Group at National Instruments Corp. His research interests include cyber-physical systems, estimation theory, navigation systems, autonomous vehicles, and intelligent transportation systems.

Zaher (Zak) M. Kassas (S'98–M'08–SM'11) is an assistant professor at the University of California, Riverside and director of the ASPIN Laboratory. He received a B.E. with Honors in Electrical Engineering from the Lebanese American University, an M.S. in Electrical and Computer Engineering from The Ohio State University, and an M.S.E. in Aerospace Engineering and a Ph.D. in Electrical and Computer Engineering from The University of Texas at Austin. From 2004 through 2010 he was a research and development engineer with the LabVIEW Control Design